Irreducible Southern Ocean State Uncertainty due to Global Ocean Initial Conditions

Hansi K.A. Singh*

School of Earth and Ocean Sciences, University of Victoria, Victoria, BC, Canada.

Naomi Goldenson

Department of Atmospheric and Oceanic Sciences, University of California at Los Angeles, Los Angeles, CA, USA.

John C. Fyfe

Canadian Center for Climate Modeling and Analysis, Victoria, BC, Canada.

Lorenzo M. Polvani

Department of Applied Physics and Applied Mathematics, and Department of Earth and Environmental Sciences, Columbia University, New York City, NY, USA.

**Corresponding author address:* Hansi K.A. Singh, School of Earth and Ocean Sciences, University of Victoria, Victoria, BC, Canada.

E-mail: hansingh@uvic.ca

ABSTRACT

How do ocean initial conditions impact historical and future climate projections in Earth system models? To answer this question, we use the 50-member Canadian Earth System Model (CanESM2) large ensemble, in which individual ensemble members are initialized using a strategic combination of different oceanic initial states and different atmospheric perturbations. We show that global ocean heat content anomalies associated with the different ocean initial states persist from initialization at year 1950 through the end of the simulations at year 2100. We also find that these anomalies most readily impact surface climate over the Southern Ocean. Ocean initial conditions affect Southern Ocean surface climate because persistent deep ocean temperature anomalies upwell along sloping isopycnal surfaces that delineate neighboring branches of the Upper and Lower Cells of the Global Meridional Overturning Circulation. As a result, up to a quarter of the ensemble variance in Southern Ocean turbulent heat fluxes, heat uptake, and surface temperature trends can be traced to variance in the ocean initial state. Such a discernible impact of varying ocean initial conditions on ensemble variance over the Southern Ocean is evident throughout the full 150 simulation years of the ensemble, even though upper ocean temperature anomalies due to varying ocean initial conditions rapidly dissipate over the first two decades of model integration over much of the rest of the globe.

1. Introduction

The Earth's climate system is variable over a range of time scales, from seconds to decades to millennia (Peixoto and Oort 1992). This abundant internal variability presents challenges for understanding the climate system's response to anthropogenic greenhouse gas emissions and other forcing agents: what part of the observed (or modeled) change in climate is due to the forcing, greenhouse gas or otherwise, and what part is due to the internal variability of the Earth system?

"Large ensembles" are an important tool for separating the forced response from internal variability. These ensembles are a sizeable collection of experiments using a single Earth System Model (ESM) subjected to identical forcings but with different initial conditions. Because two ESM integrations forced identically will diverge even if they start from a nearly identical initial state, such a large ensemble may be used to create an array of possible climate trajectories. Differences between ensemble members are then attributable solely to internal variability in the model, while the mean evolution of all ensemble members is attributable to the forcing. In this framework, the actual trajectory of the Earth's climate is just one of many possible trajectories that might arise from the applied forcing in a perfect model.

Large ensembles show that internal variability lends substantial uncertainty to future climate projections (Deser et al. 2012, 2014). In the 40-member Community Earth System Model Large Ensemble (CESMLE; see Kay et al. 2015), for example, individual ensemble members exhibit significantly different global mean surface temperature trends even a century after initialization, and regional surface temperature trends show even greater variance between members. In the Arctic, where internal variability is particularly large, analysis of large ensembles suggests that much of the observed total sea ice area decline, warming, and changes in precipitation are attributable to greenhouse gas forcing (Screen et al. 2014). However, variability in the atmospheric circulation may still account for up to half the observed downward trend in summer sea ice (Ding et al. 2017), since circulation changes that accompany Arctic warming are difficult to distinguish from internal variability (Screen et al. 2014; Wettstein and Deser 2014). Moreover, local trends in sea ice area are only attributable to greenhouse gas forcing in certain regions and over certain seasons (England et al. 2019). Indeed, the precise timing of a sea ice-free Arctic in summer depends largely on the sequence of internal variability in a given ensemble member (Swart et al. 2015), and may depend very little on the emissions scenario (Jahn et al. 2016). Other studies show that internal variability is significant for such varied climate change indicators as Hadley Cell expansion (Kang et al. 2013), atmospheric river landfall frequency (Hagos et al. 2016), and Southern Ocean carbon uptake (Lovenduski et al. 2016).

Because large ensembles have become an indispensable tool for understanding how the climate system evolves in the presence of internal variability, it is reasonable to consider just how these ensembles are constructed. Thus far, there are two commonly used methods for creating initial conditions to spawn large ensembles (as described by Stainforth et al. 2007): micro-initialization, using tiny perturbations (i.e., of a magnitude similar to machine round-off error) in the atmospheric initial state; or macro-initialization, using different ocean starting states sampled from a long control run. Because large ensembles generally use either atmospheric micro-perturbations (see, for example, the CESMLE; Kay et al. 2015) or varying ocean initial conditions (see, for example, the MPI Grand Ensemble; Maher et al. 2019) for their ensemble initialization, it is unclear whether the two methods yield a similar range of internal variability and, therefore, a similar spread in climate projections. Because each ESM has its own representation of internal climate variability, macro-initialization and micro-initialization would need to be applied in the same ESM in order to compare their impact on ensemble variance.

The importance of the ocean state for driving Earth system evolution is already well recognized in other applications. In the field of decadal climate predictability, accurate ocean state initialization is of prime importance in determining the climate's trajectory (see, for example, Latif and Keenlyside 2011; Bellucci et al. 2013; Meehl et al. 2014; Yeager and Robson 2017, and many others). Initialization of coupled climate models with a given phase of the Atlantic Multidecadal Oscillation (AMO), Pacific Decadal Oscillation (PDO), or both, partly determines the evolution of ocean temperature, salinity, and sea surface height over one or more decades (see, for example, Griffies and Bryan 1997; Rodwell et al. 1999; Mochizuki et al. 2012; Chikamoto et al. 2013), and may enhance predictability of the extratropical circulation, the hydrologic cycle, and tropical Atlantic variability over seasonal, interannual, and decadal time scales (see, for example, Dunstone et al. 2011; Simpson et al. 2019; Athanasiadis et al. 2020). Furthermore, climate model experiments also suggest that the ocean state may help drive multidecadal trends in Antarctic sea ice, including the expansion of Antarctic sea ice area over the satellite era (1979 to 2015; see Cavalieri et al. 1996, updated yearly): some have suggested that tropical-extratropical teleconnections mediated by the Interdecadal Pacific Oscillation may have facilitated Antarctic sea ice expansion over that period (Meehl et al. 2016), while others have pointed to the state of the Southern Ocean as the implicating factor (see Zhang et al. 2019; Singh et al. 2019).

Given this wealth of evidence that the ocean state impacts climate evolution, it is reasonable to hypothesize that large ensembles initialized from many different ocean states may exhibit variability not found in those initialized from a single ocean state. Indeed, one prior study exploring the matter suggests that initializing a large ensemble with a range of ocean initial conditions increases ensemble variance beyond that possible with only atmospheric micro-perturbations. Hawkins et al. (2016) used an Earth system Model of Intermediate Complexity (EMIC) to show that a historically-forced large ensemble starting from several distinct ocean initial states displayed significantly greater variance in global and regional temperature trends, even a century after initialization, compared to one starting from only a single ocean initial state. More specifically, the phase of the Atlantic Meridional Overturning Circulation from which an ensemble member was initialized influenced northern hemispheric temperature trends, particularly in those regions proximal to the North Atlantic. Because these experiments utilized an EMIC rather than an ESM, however, there remains a question of whether such increased variability is a product of the greater sensitivity of simpler models to parameter and initial condition perturbations (such as is the case for sea ice instability; see Wagner and Eisenman 2015), or whether such increased variability is also found in large ensembles of more comprehensive Earth system models. In other words, is ESM ensemble variance also amplified by initializing members from different ocean states, compared to initializing members with atmospheric micro-perturbations alone?

In this study, we address this very question. We analyze the Canadian Earth System Model version 2 (CanESM2; Arora et al. 2011) large ensemble, run with historical and RCP8.5 future scenario forcings (Taylor et al. 2012; Deser et al. 2020) from 1950 to 2100. This large ensemble is composed of five micro-ensembles (consisting of 10 ensemble members each), where individual members of a given micro-ensemble are initialized from an identical ocean state, but each micro-ensemble is initialized from a distinct ocean state. The unique structure of this 50-member large ensemble permits us to decompose the variance in the ensemble into a component due to the ocean initial state, and a component due to atmospheric micro-perturbations alone.

We begin our analysis of the CanESM2 large ensemble by evaluating how ocean initial conditions, including potential temperature and ocean heat content, differ between micro-ensembles (§3a). We then show how the ocean state evolves from 1850 to 2100 in each micro-ensemble, and compute the extent to which ocean potential temperature variance in the full ensemble can be attributed to different ocean initial conditions (§3b). Finally, we demonstrate that it is over the Southern Ocean where such initial conditions continue to impact ensemble variance in surface climate, up to 150 years following model initialization in 1950 (§3c). In §4, we conclude by discussing the implications of our findings for the design of large ensembles, and how climate system predictability may be limited by our imperfect knowledge of prior ocean states.

2. Methods

The Canadian Earth System Model, version 2 (hereafter CanESM2) is state-of-the-art, fully-coupled, and has atmosphere, ocean, sea ice, and land components (described in detail in Arora et al. 2011). The atmosphere model, CanAM4 (von Salzen et al. 2013), utilizes a spectral dynamical core at T63 truncation, with a resolution of 1.875° at the equator; there are 35 vertical levels which extend to 1 hPa. New parameterizations include a correlated-*k* radiative transfer scheme (Li and Barker 2005), a prognostic bulk aerosol treatment (Ma et al. 2010), and single-moment cloud microphysics (Khairoutdinov and Kogan 2000). The ocean model has 40 vertical levels with a nominal horizontal resolution of 1°. It utilizes the K-profile parameterization for vertical mixing at the boundary layer (Large et al. 1994) and the GM90 parameterization for mixing by sub-grid scale eddies along isopycnal surfaces (Gent and McWilliams 1992). The sea ice model is fully dynamic and thermodynamic, and both the land and ocean models include a prognostic carbon cycle (Christian et al. 2010).

CanESM2 compares favorably with other models participating in the 5th phase of the Climate Model Intercomparison Project (CMIP5; see Taylor et al. 2012), in terms of its representation of both mean state climate and internal variability over seasonal to centennial time scales (Flato et al. 2014). Further studies indicate reasonable simulation of coupled modes of climate variability, including ENSO (see, e.g., Bellenger et al. 2014) PDO (see, e.g., Yim et al. 2015), and Southern Hemispheric extratropical circulation features (including SAM, jet position, and location of the maximum westerly wind stress; see Thomas et al. 2015). CanESM2 also simulates both the mean state and variability of meridional ocean heat transport well, including its gyre and overturning components (see Yang and Saenko 2012).

As illustrated in Figure 1, ocean initial conditions for the 50-member CanESM2 large ensemble are constructed by branching 5 runs from different points in an 1850s pre-industrial control experiment (Kirchmeier-Young et al. 2017). The first of the 5 branches starts after 2271 model-years of the pre-industrial control simulation, and subsequent branches each begin 50 years after the previous branch (years 2321, 2371, 2421, and 2471). The pre-industrial control has a top-of-atmosphere anomaly of 0.17 W m^{-2}, and the deep ocean is drifting by approximately -0.05 K (100 yrs)$^{-1}$ (as documented for CMIP5-participating models in Hobbs et al. 2016). Because of this deep ocean drift, there is approximately a 0.2K range in deep ocean temperatures (below 1500m) between these branches.

Each of these five branches is subjected to identical historical forcings from years 1850 to 1950. At year 1950, each of the 5 branched runs is subjected to ten distinct sets of random microperturbations in the atmosphere (by using 10 different pre-set seeds for a random number generator employed in the model's cloud microphysics parameterization) to produce 10 ensemble members each. Hereafter, we use the term *'micro-ensemble'* to refer to each set of 10 ensemble members that shares an identical ocean initial state at year 1950. As per the protocol of the fifth phase of the Climate Model Intercomparison Project (CMIP5; see Taylor et al. 2012), all of these ensemble members are subjected to identical historical forcings (from 1950 to 2005) and the RCP8.5 scenario forcing (from 2006 to 2100, to yield a total nominal greenhouse gas forcing of 8.5 W m^{-2} by the end of the 21st century, relative to the pre-industrial).

a. Decomposition of Ensemble Variance

We now describe the process by which we estimate how much variance in the whole ensemble is attributable to ocean initial conditions, and how much is attributable to atmospheric micro-perturbations.

The variance σ_X^2 in a climatically-relevant quantity X (such as temperature, surface fluxes, ocean heat content, or others) between all ensemble members over a given year is computed as

$$\sigma_X^2(t) = \frac{\sum_{i=1}^{n}(X(t) - \overline{X}(t))^2}{n-1} \ , \tag{1}$$

where $\overline{X}(t)$ is the average of X across all ensemble members at year t, and n is the number of ensemble members (equal to 50 in the CanESM2 large ensemble). While this can be a function of time, we drop this time-dependent notation in the following description for the sake of clarity.

The total variance between ensemble members over a given year can be approximated as the sum of two variances: (1) the variance between micro-ensembles, due to the different ocean states used to initialize each micro-ensemble, is denoted by $\sigma^2_{X,ocean}$; and (2) the variance within micro-ensembles, due to application of different atmospheric micro-perturbations in each ensemble member, is denoted by $\sigma^2_{X,atmos}$. In other words,

$$\sigma_X^2 = \sigma^2_{X,ocean} + \sigma^2_{X,atmos} + \varepsilon \ . \tag{2}$$

In equation (2) above, the error, ε, includes the nonlinear interaction term; ε generally constitutes less than 5% of the total variance, which we drop for convenience. This approximation, inspired by the decomposition of variance performed by Hawkins and Sutton (2009), makes sources of ensemble variance simple to compute and easy to attribute, to first-order.

The variance within micro-ensembles, $\sigma^2_{X,atmos}$ is computed as the average of the variance within each micro-ensemble:

$$\sigma^2_{X,atmos} = \frac{1}{p}\sum_{k=1}^{p}\frac{\sum_{j=1}^{m}(X_{k,j}-\overline{X_k})^2}{m-1}\ , \tag{3}$$

where $X_{k,j}$ is the value of X in the j-th member of the k-th micro-ensemble, and $\overline{X_k}$ is the mean of X in micro-ensemble k. In the above equation, m is the number of ensemble members in each micro-ensemble (equal to 10 for the CanESM2 large ensemble), and p is the number of micro-ensembles (5 for the CanESM2 large ensemble). The variance between micro-ensembles, $\sigma^2_{X,ocean}$, is computed as the variance of the individual micro-ensemble means:

$$\sigma^2_{X,ocean} = \frac{\sum_{k=1}^{p}(\overline{X_k}-\overline{X})^2}{p-1}\ , \tag{4}$$

where $\overline{X}$ is the mean of X in the entire ensemble (i.e. over all 50 members of the CanESM2 large ensemble).

Because individual ensemble members within each micro-ensemble all start with identical ocean initial conditions at year 1950, the variance within micro-ensembles, $\sigma^2_{X,atmos}$, is attributable solely to initial micro-perturbations (on the order of machine error) in the surface atmospheric temperature. Similarly, the variance between micro-ensembles, $\sigma^2_{X,ocean}$, arises from the different ocean initial conditions in each micro-ensemble; by considering the variance of the micro-ensemble means, the impact of varying atmospheric micro-perturbations is averaged out. The fraction of the ensemble variance in X due to ocean initial conditions at time t can then be written as follows:

$$\chi_{OcnICs}(t) = \frac{\sigma^2_{X,ocean}(t)}{\sigma^2_X(t)} \tag{5}$$

We label $\chi_{OcnICs}(t)$ as statistically distinct from zero using a bootstrapped 90%-confidence approach as follows. For 100 realizations, we randomly assign each of the 50 ensemble members into 5 micro-ensembles of 10 members each, and recompute the variance between micro-ensembles ($\widetilde{\sigma^2}_{X,between}$) and within micro-ensembles ($\widetilde{\sigma^2}_{X,within}$). These randomly-resampled micro-ensembles are synthetic, in that their members do not share the same ocean initial conditions as do members of the original micro-ensembles. Therefore, non-zero values of $\widetilde{\sigma^2}_{X,between}$ are attributable solely to chance, not to ocean initial conditions. We repeat the above randomization a total of 100 times, to get 100 synthetic realizations of $\widetilde{\sigma^2}_{X,between}$, to compare to the variance between the real micro-ensembles, $\sigma^2_{X,ocean}$. We treat $\sigma^2_{X,ocean}$ as statistically different from zero if $\sigma^2_{X,ocean} > \widetilde{\sigma^2}_{X,between}$ at least 90% of the time, accepting a 10% possibility that the difference could be due to chance. We use a 90% confidence level, rather than the more customary 95% level, in order to avoid type II errors that are more likely to arise when comparing the variance of two quantities (see Von Storch and Zwiers 2001).

3. Results

a. Ocean Initial Conditions in the CanESM2 Large Ensemble

We begin by examining how ocean initial conditions at year 1950 vary between micro-ensembles. Figure 2 shows the anomaly in the mean (zonally-averaged) ocean potential temperature in each micro-ensemble, relative to the mean over all ensemble members (i.e. $[\overline{\theta_k}] - [\overline{\theta}]$, where $[\overline{\theta_k}]$ is the average zonal-mean potential temperature in micro-ensemble k, and $[\overline{\theta}]$ is the average zonal-mean potential temperature in the full 50-member ensemble). At year 1950, there are several key areas where ocean initial temperatures differ significantly between micro-ensembles: within the Arctic basin (poleward of 75N), in the northern hemisphere subpolar oceans (between 60N and 75N), and in the global deep ocean (below 1.5 km depth at latitudes south of 60N). Further differences are also apparent in the upper ocean (above 500 m), particularly in the tropics and over the Southern Ocean (poleward of 45S). While upper ocean temperature differences between micro-ensembles arise from internal variability, deep ocean temperature differences are generated by drift in the pre-industrial control experiment (see §2).

We further note that there is little coherence between anomalies over different areas: individual micro-ensembles are neither uniformly cooler than average globally nor uniformly warmer. For example, cool temperatures in the subpolar northern hemisphere may be associated with either cool anomalies in the global deep ocean (as in micro-ensemble 1; Fig 2a) or warm anomalies (as in micro-ensemble 5; Fig 2e).

In Figure 3, we show the average initial ocean heat content anomaly per unit area (in 10^9 J m^{-2}) in each micro-ensemble, relative to the average over the full ensemble (i.e. $\overline{OHC}_k - \overline{OHC}$). As expected, anomalies in ocean potential temperature result in significant differences in ocean heat content between micro-ensembles. Over most latitudes, the average heat content anomaly in each micro-ensemble is consistent with the potential temperature anomaly in the deep ocean (below 1.5 km): anomalously cool deep ocean temperatures in micro-ensemble 1 (Fig 2a) are accompanied by lower than average ocean heat content over much of the globe (Fig 3a), while anomalously warm deep ocean temperatures in micro-ensemble 5 (Fig 2e) are accompanied by higher than average ocean heat content. Though anomalies in potential temperature in the deep ocean are small (below 2 km depth, there is less than a 0.2K difference between micro-ensembles 1 and 5, as shown in Fig 2), ocean heat content anomalies are substantial (on the order of 10^9 J m^{-2}) because of the enormous volume of the deep ocean.

b. Ocean Evolution in the CanESM2 Large Ensemble

In Figure 4, we show the evolution of global ocean heat content from 1950 to 2100 in each micro-ensemble, $\overline{OHC}_k$ (relative to the ensemble mean global ocean heat content from 1950 to 1970). At year 1950, the average global ocean heat content in each micro-ensemble, relative to that in other micro-ensembles, is consistent with the temperature and ocean heat content anomalies shown previously (recall Figs 2 and 3). For example, micro-ensemble 1 has, on average, the most anomalously cold deep ocean temperatures (Fig 2a) and the lowest ocean heat content per unit area (Fig 3a), relative to other micro-ensembles; therefore, unsurprisingly, its average global ocean heat content is the lowest of the five micro-ensembles (Fig 4a, thick dark blue line). Similarly, micro-ensemble 5 has, on average, the most anomalously warm deep ocean temperatures and highest ocean heat content per unit area, giving it the greatest average global ocean heat content of all micro-ensembles (Fig 4a, thick dark red line). The total range in global ocean heat content between micro-ensemble means is approximately 350 ZJ at year 1950 (Fig 4b; difference between thick dark red and dark blue lines).

The global ocean heat content remains relatively constant from years 1950 to 1980 in all ensemble members, but begins to increase after year 1980 (Figure 4a). The rate at which global ocean heat content increases is not constant in time, but accelerates in all micro-ensembles (Fig 4a; the ocean heat content time series have positive curvature) as the forcing and rate of ocean heat uptake increase (Shi et al. 2018). As such, by year 2100, the global ocean heat content has increased by approximately 3500 ZJ due to (historical and RCP8.5) forcings which have warmed the planet and increased global ocean temperatures.

Of particular note in Figure 4b is that the ordering of the average global ocean heat content anomaly in each micro-ensemble, $\overline{OHC_k} - \overline{OHC}$, remains constant with respect to other micro-ensembles throughout the 150 years of the experiment: for example, the average global ocean heat content in micro-ensemble 2 is always greater than that in micro-ensemble 1 (i.e. $\overline{OHC_1}(t) < \overline{OHC_2}(t)$ for all t) and less than that in micro-ensembles 3 through 5 (i.e. $\overline{OHC_2}(t) < \overline{OHC_{3,4,5}}(t)$ for all t). This is also evident in individual ensemble members within each micro-ensemble: for example, the global ocean heat content anomalies in individual ensemble members from micro-ensemble 1 (Fig 4b, thin dark blue lines) are always less than those in individual ensemble members in micro-ensemble 2 (Fig 4b, thin light blue lines). Indeed, only micro-ensembles 3 and 4 show significant overlap between ocean heat content in individual ensemble members (Fig 4b, compare thin grey and pink lines), though their micro-ensemble means never overlap during the 150 year experiment. Furthermore, the range of the micro-ensemble means remains relatively constant at 350 ZJ up to year 2100, though the range of individual ensemble members adds approximately 50 ZJ in additional variance over the course of the experiment (Fig 4b, compare range of thick lines to range of thin lines).

Figure 5 shows that the average global ocean heat content remains distinct in each micro-ensemble because the mean potential temperature anomaly in the deep ocean in each micro-ensemble ($\overline{\theta_k}(t) - \overline{\theta}(t)$; below 1.5 km) persists through the full 150 years of the experiment. Micro-ensembles 1 and 2 always have cooler than average deep ocean potential temperature anomalies from 1950 to 2100 (Figs 5a and b), though the magnitude of these cool anomalies appears to dissipate somewhat with time (particularly in micro-ensemble 1; see Fig 5a). Similarly, micro-ensembles 4 and 5 have warmer than average deep ocean potential temperature anomalies, with larger anomalies near year 1950 than year 2100 (Figs 5d and e). Unlike the deep ocean, upper ocean potential temperatures (above 1 km) do not persist for nearly so long: in all micro-ensembles, most coherent upper ocean potential temperature anomalies have dissipated by year 2000. Even though upper ocean temperatures dissipate over the course of several decades, the average global ocean heat content anomalies in each micro-ensemble (and their constituent individual ensemble members) remain constant with time relative to each other because small (of magnitude 0.1 K) potential temperature anomalies in the deep ocean persist over century-long timescales.

Figure 6 shows the mean potential temperature anomaly at 2080 in each micro-ensemble relative to that in the full ensemble (i.e., $\overline{\theta_k}(t=2080)-\overline{\theta}(t=2080)$), which illustrates how the deep ocean temperature differences identified at year 1950 (recall Fig 2) persist over centennial timescales. In all micro-ensembles, the deep ocean temperature anomalies (below 2000 m and south of 60N) at year 2080 are of the same sign as those at year 1950, albeit of somewhat weaker magnitude (compare micro-ensembles in Fig 6 with same micro-ensembles in Fig 2; note that the colorbar range is twice as large in Fig 2 as in Fig 6). On the other hand, upper ocean temperature anomalies in individual micro-ensembles are substantially weaker at year 2080 than at year 1950, and are generally not of the same sign or spatially coherent with those at the start of the experiment. In the Arctic basin (poleward of 70N), we do find some evidence of coherence in temperature anomalies from 1950 and 2080, though not in all micro-ensembles: potential temperature anomalies are of the same sign through the course of the experiment in micro-ensembles 1, 3, and 4, but are of different (or mixed) sign in ensembles 2 and 5.

1) Attribution of Ocean State Evolution to Atmosphere and Ocean Initial States

We now compute the fraction the total variance in ocean potential temperature in the CanESM2 large ensemble that is attributable to ocean initial conditions, $\chi_{OcnICs} = \sigma^2_{\theta,\ ocean}/\sigma^2_{\theta}$ (i.e. the fraction of the total ensemble variance that is between micro-ensembles, as detailed in Decomposition of Ensemble Variance in Methods). Figure 7 shows this quantity from four 20-year periods over the course of the experiment, and Figure 8 shows a closer view of the top 2000 m of the water column. Early in the experiment (from years 1950 to 1970; Figs 7a and 8a), most ensemble variance in ocean potential temperature below 1500 m is between micro-ensembles (i.e. $\sigma^2_{\theta,\ ocean} \gg \sigma^2_{\theta,\ atmos}$; note red and orange colors), indicating that it is attributable to the different ocean initial conditions in each micro-ensemble. Even in the upper ocean (above 1000 m), at least half of the ensemble variance is attributable to these differences in ocean initial conditions, though this varies by latitude and depth.

By years 1980 to 2000 (Figs 7b and 8b) and beyond (Figs 7c and d; Figs 8c and d), much of the ensemble variance in upper ocean potential temperatures (above 1000 m at most latitudes) is no longer attributable to differences between ocean initial states, but rather to atmospheric variability (note hatched blue and green areas, where the fraction of the variance attributable to ocean initial conditions is not statistically distinct from zero). At some latitudes, atmospheric variability penetrates even deeper into the ocean: in the subpolar northern hemisphere, circa 60N; and in the deep Southern Ocean, poleward of 60S below 2000 m. This occurs because the subpolar North Atlantic and the Antarctic continental shelves are locales of weak vertical stratification and deep convection, which allows atmospheric anomalies to penetrate to depth at these latitudes. Indeed, we observe that the variance attributable to ocean initial conditions steadily decreases with time in the deep Southern Ocean (compare, in succession, Figs 7b, c, and d), as anomalies attributable to atmospheric variability penetrate further into the deep ocean along the descending branch of the deep overturning cell (Fig 7, dotted purple lines).

On the other hand, nearly all ensemble variance in deep ocean temperatures, north of 50S, is attributable to ocean initial conditions over the full 150 years of the experiment (Fig 7, dark red regions below 2000 m). These persistent deep ocean temperature anomalies appear to be isolated from the surface at most latitudes, as only a small fraction of upper ocean temperature variance is attributable to ocean initial conditions. Therefore, persistent deep ocean temperature anomalies (recall Figs 5 and 6) do not impact surface climate directly. Indeed, the upper ocean is highly stably stratified at most latitudes (Peixoto and Oort 1992), which effectively isolates deep ocean waters from those nearer the surface.

However, in the upper ocean between 60S and 70S, we find that approximately 50% of ensemble variance is between micro-ensembles over all time periods (Fig 8a-d), and is therefore attributable to differences in ocean initial conditions. Indeed, we note a 'plume'-like feature that emerges from the deep ocean circa 2500 m, near 50S, where most ensemble variance is due to ocean initial conditions, and follows sloping isopycnal surfaces to the upper ocean near 65S (see orange and yellow shaded regions between black contours in Figs 7 and 8). This feature is apparent over all time periods shown (though it does appear to weaken with time; compare Figs 8b and d), and is coincident with climatological upwelling of deep waters in the ascending branch of the lower cell of the oceanic meridional overturning circulation (Figs 7 and 8, dashed pink contour at -4×10^9 kg sec^{-1}; also see Marshall and Speer 2012). In other words, the lower cell of the meridional overturning circulation transports deep ocean temperature anomalies, attributable to ocean initial conditions, into the upper ocean circa 65S. As a result, the Southern Ocean, between 55S and 70S, is the primary locale where surface conditions are impacted directly by persisting deep ocean temperature anomalies, which are due to differences in ocean initial conditions between micro-ensembles.

We also note that only about half of the temperature variance in the Southern Ocean upwelling branch of the overturning circulation is attributable to ocean initial conditions (particularly over longer time scales; see Figs 8b, c, d). This suggests that while persistent deep ocean temperature anomalies upwell along sloping isopycnal surfaces, adiabatic eddies also transport temperature anomalies from the surface to depth along these same isopycnal surfaces (see Gent and McWilliams 1992; Marshall and Speer 2012). Mixing with equatorward-flowing Antarctic intermediate and Sub-antarctic mode waters (Rintoul 1991) likely also contributes further atmosphere-sourced temperature variance to these upwelling waters. Therefore, temperature anomalies that upwell from the deep ocean are responsible for about half the ensemble variance, while the rest is attributable to variability generated by atmospheric temperature anomalies mixed down from the surface.

c. Impact on Surface Climate

We now consider the impact of ocean initial conditions on ensemble variance in surface climate, focusing on quantities central to the forced evolution of the ensemble. These include upper ocean heat content, surface temperature trends, and air-sea fluxes which govern the rate at which the ocean takes up excess heat. As described above, persistent deep ocean temperature anomalies (attributable to differences in ocean initial conditions, as shown in Figs 7 and 8) primarily affect upper ocean temperature variance between 55S and 75S. As expected, we find the greatest fraction of variance in upper ocean heat content (reckoned from the surface to 300 m depth) attributable to ocean initial conditions circa these same Southern Ocean latitudes (Fig 9a, which shows $\chi_{OcnICs} = \sigma^2_{OHC,\ ocean}/\sigma^2_{OHC}$; note area between pink horizontal lines, which delineate the Southern Ocean). This is evident over the entire course of the experiment, though it is greatest near the beginning of the experiment (circa year 1960), decreases thereafter, but increases again between years 2055 to 2095.

The primary mechanism by which converging ocean heat impacts the surface climate is through changes in surface turbulent (sensible and latent heat) fluxes (Sutton and Mathieu 2002). This relationship is apparent from the physics that governs evolution of the ocean mixed layer temperature, T_o:

$$\rho c_w h_{ML} \frac{dT_o}{dt} = \rho c_w h_{ML} \vec{v} \cdot \nabla T_o + Q_{sfc}(T_o) \ , \tag{6}$$

where ρ is the density of seawater, c_w is its heat capacity, h_{ML} is the mixed layer depth, $\vec{v}$ is the advective velocity, and $Q_{sfc}(T_o)$ is the sum of the surface fluxes (positive into the ocean). In brief, the temperature evolution of the upper ocean depends on convergent temperature advection by fluid flow ($\rho c_w h_{ML} \vec{v} \cdot \nabla T_o$) and energy loss or gain through surface fluxes ($Q_{sfc}(T_o)$). Therefore, temperature anomalies that upwell from the deep drive the evolution of upper Southern Ocean temperatures, which then further impact surface fluxes. Turbulent surface fluxes, in particular, depend on the temperature difference between the ocean surface and overlying atmosphere, indicating that these respond to changes in upper ocean temperature.

Indeed, we find that the Southern Ocean, between 45S and 70S, is the locale where the greatest fraction of ensemble variance in latent heat fluxes is consistently attributable to ocean initial conditions (i.e., is due to variance between micro-ensembles; Fig 9b, which shows $\chi_{OcnICs} = \sigma^2_{F_{LH},\ ocean}/\sigma^2_{F_{LH}}$; note area between pink horizontal lines, which delineates the Southern Ocean). Furthermore, the fraction of ensemble variance in Southern Ocean latent heat fluxes attributable to ocean initial conditions fluctuates with time similarly to the upper Southern Ocean heat content: greatest from 1960 to 2000, weaker thereafter, and increasing again from 2050 to 2090 (compare Figs 9a and b). However, the fraction of ensemble variance attributable to ocean initial conditions for latent heat fluxes is substantially smaller than for upper ocean heat content: only between 10% to 15% of the ensemble variance in Southern Ocean latent heat fluxes, compared to 15% to 25% for upper Southern Ocean heat content, is attributable to ocean initial conditions.

Similarly, surface temperature trends over the Southern Ocean also exhibit significant variance due to ocean initial conditions (Fig 9c, which shows $\chi_{OcnICs} = \sigma^2_{dT_s/dt,\ ocean}/\sigma^2_{dT_s/dt}$; note area between pink horizontal lines) because upper ocean heat convergence impacts the ocean temperature tendency, dT_o/dt (recall equation 6). Like the ensemble variance in latent heat fluxes described above, the variance in Southern Ocean surface temperature trends also fluctuates with time similarly to the upper ocean heat content variance, and is also weaker in magnitude.

In Figure 10, we examine surface flux anomalies (from 55S to the pole) over four time periods in each micro-ensemble, calculated as the difference between the micro-ensemble mean and the full ensemble mean (i.e. $\overline{F_{X,\,k}}(t) - \overline{F_X}(t)$). We find systematic differences between turbulent fluxes, both latent (F_{LH}; Fig 10a) and sensible (F_{SH}; Fig 10b), in micro-ensembles with colder-than-average deep ocean temperatures (micro-ensembles 1 and 2) compared to those with warmer-than-average deep ocean temperatures (micro-ensembles 4 and 5). When deep ocean temperatures are anomalously cold, as in micro-ensembles 1 and 2, both latent and sensible heat fluxes are anomalously low relative to the full ensemble mean over all time periods (Figs 10a and b, dark and light blue markers; $\overline{F_{X,\,1,2}}(t) < \overline{F_X}(t)$); conversely, when deep ocean temperatures are anomalously warm, as in micro-ensembles 4 and 5, turbulent fluxes are anomalously high (Figs 10a and b, pink and red markers; $\overline{F_{X,\,4,5}}(t) > \overline{F_X}(t)$). The sign of these turbulent flux anomalies in each micro-ensemble is consistent with the sign of the deep ocean temperature anomalies reported earlier (recall $\overline{\theta_k}(t) - \overline{\theta}(t)$ in Figs 2, 5, and 6): when warmer deep ocean temperature anomalies advect into the upper ocean, we find ocean heat content and turbulent heat fluxes to be higher than the ensemble average (as in micro-ensembles 4 and 5); on the other hand, when cooler deep ocean temperature anomalies advect into the upper ocean, we find that ocean heat content is lower than average and turbulent heat fluxes are weak (as in micro-ensembles 1 and 2).

Differences in Southern Ocean turbulent fluxes between micro-ensembles, attributable to deep ocean temperature differences, also impact the ocean heat uptake (OHU). The rate of deep ocean heat uptake is central to the forced transient climate response (Boé et al. 2009; Kuhlbrodt and Gregory 2012), and the Southern Ocean is the locale where most of this heat uptake occurs (Frölicher et al. 2015; Shi et al. 2018). The ocean heat uptake is computed as

$$OHU = R^{\downarrow}_{SW+LW} - F_{SH} - F_{LH}\ , \tag{7}$$

where $R^{\downarrow}_{SW+LW}$ is the net (downward, shortwave plus longwave) radiative flux at the surface. In micro-ensembles 1 and 2 where mean deep ocean temperatures are anomalously cool compared to the ensemble mean, turbulent heat fluxes over the Southern Ocean are weaker than the ensemble mean, and ocean heat uptake is greater than the ensemble mean over all time periods (Fig 10c, dark and light blue markers; $\overline{OHU_{1,2}}(t) > \overline{OHU}(t)$). Similarly, in micro-ensembles 4 and 5 where mean deep ocean temperatures are anomalously warm compared to the ensemble mean, turbulent heat fluxes are more vigorous than the ensemble mean, and ocean heat uptake is weaker than the ensemble mean over all time periods (Fig 10c, red and pink markers; $\overline{OHU_{4,5}}(t) < \overline{OHU}(t)$). In other words, persistent cool anomalies in the deep ocean tend to augment ocean heat uptake with CO_2 forcing, while persistent warm anomalies in the deep ocean tend to suppress ocean heat uptake.

In CanESM2, the micro-ensemble mean ocean heat uptake anomaly scales approximately one-to-one with the initial micro-ensemble mean deep ocean temperature anomaly:

$$\frac{\overline{OHU_k}(t) - \overline{OHU}(t)}{\overline{T_{deep,\,k}}(t = 1950) - \overline{T_{deep}}(t = 1950)} \sim -1 \text{ W m}^{-2} \text{ K}^{-1} \, . \tag{8}$$

For example, an initial mean deep ocean temperature anomaly of -0.1K, as in micro-ensemble 1, gives rise to approximately a 0.1 W m^{-2} mean anomaly in ocean heat uptake in micro-ensemble 1 over the first 100 years of the experiment (i.e. from 1950 to 2000, and from 2000 to 2050; Fig 10). We note that this scaling depends on the rate at which the ocean meridional overturning upwells anomalies from the deep ocean, which varies substantially between global climate models (see, for example, Behrens et al. 2016).

Though it is clear that Southern Ocean heat uptake is sensitive to differences in deep ocean temperature between micro-ensembles, we note that the ensemble range (i.e. the total ensemble spread, which is attributable to both atmospheric micro-perturbations and ocean initial condition differences) becomes substantially smaller over time relative to the forced response. Over years 1950 to 2000, the ensemble range in Southern Ocean heat uptake is of similar magnitude to the forced change: both are approximately 0.5 W m^{-2}. Over years 2000 to 2050, the ensemble range in Southern Ocean heat uptake decreases slightly to approximately 0.4 W m^{-2}, but greenhouse gas forcing has now increased ocean heat uptake over this region to 1.7 W m^{-2}. By years 2050 to 2100, the ensemble range is only a small fraction of the forced response in Southern Ocean heat uptake: the ensemble range is still approximately 0.4 W m^{-2}, but the forced change over the region has increased to 3.8 W m^{-2}, so uncertainty due to internal variability is only about 10% of the forced response. Thus, though ensemble spread (due to internal variability stemming from both macro- and micro-initialization) contributes to uncertainty in Southern Ocean heat uptake over centennial time scales, it is likely that other sources of uncertainty (including that due to model physics and emissions scenario) are responsible for most of the uncertainty over these time scales (Hawkins and Sutton 2009).

In Figure 11, we examine the variance in Southern Ocean heat uptake (from 55S to the pole, as in Fig 10c) between micro-ensembles ($\sigma^2_{OHU,\ ocean}$; blue lines) and within micro-ensembles ($\sigma^2_{OHU,\ atmos}$; purple lines). The total variance in the ocean heat uptake appears to decrease slightly over the first several decades, but thereafter remains relatively constant (Fig 11a, black line). This suggests greater ensemble variance attributable to ocean initial conditions at the beginning of the experiment (approximately 30% over the first 50 years; Fig 11b), and less ensemble variance attributable to ocean initial conditions near the end of the experiment (approximately 20% over the final 50 years). We note that the fraction of the ensemble variance in ocean heat uptake attributable to ocean initial conditions does not dwindle to zero because deep ocean temperature differences between micro-ensembles continue to persist even at year 2100. Given the modest rate of Southern Ocean upwelling (of order 10^9 kg sec^{-1}; recall Fig 7) and the enormous volume of the deep ocean (of order 10^8 km^3), these deep ocean temperature anomalies can be expected to persist for over 10^3 years. As long as these deep ocean temperature anomalies exist, we expect that they will continue to impact surface fluxes over the Southern Ocean, albeit more modestly with time as their magnitude declines.

4. Discussion

In this study, we have used the CanESM2 large ensemble to answer a simple, but important, question: how much do varying ocean initial conditions impact variance in ESM large ensembles? To answer this, we have harnessed the macro-micro structure of the CanESM2 large ensemble, first of its kind among full-complexity climate models, to separate ensemble variance due to ocean initial conditions from that due to atmospheric micro-perturbations. We find that deep ocean potential temperature anomalies associated with different ocean initial conditions persist for at least 150 years following model initialization, and that these anomalies primarily impact surface climate over the Southern Ocean as they upwell to the surface along the ascending branch of the lower cell of the ocean meridional overturning circulation. In turn, some ensemble variance in Southern Ocean heat content (from the surface to 300m depth), turbulent heat fluxes, temperature trends, and ocean heat uptake is attributable to ocean initial conditions. In other words, using a range of ocean states to initialize a large ensemble increases uncertainty in how the Southern Ocean evolves, which is arguably the region that is most consequential for determining the pace of climate change. Though these impacts on surface climate are localized to the Southern Ocean and modest in magnitude, they are persistent over the full 150 years of the ensemble, and suggest that uncertainties in Southern Ocean surface climate due to uncertainties in ocean initial conditions can be expected to persist over at least 150 years and likely longer.

Most striking is the strength of the relationship between mean deep ocean temperature anomalies ($\overline{T_{deep,\,k}} - \overline{T_{deep}}$) and mean Southern Ocean heat uptake anomalies in a given micro-ensemble ($\overline{OHU_k} - \overline{OHU}$): we find that a 1 K anomaly in deep ocean temperatures in a micro-ensemble, relative the full ensemble mean, would result in a -1 W m^{-2} anomaly in Southern Ocean heat uptake in that micro-ensemble relative to full ensemble mean (recall equation 8). We expect that this relationship is model-dependent, as the rate of upwelling of deep ocean temperature anomalies by the ocean meridional overturning circulation will determine the magnitude of the upper ocean heat content anomaly due to these deep ocean anomalies and, therefore, their impact on surface turbulent fluxes. Furthermore, the time scales over which deep ocean temperature anomalies persist, and continue to impact surface fluxes over the Southern Ocean, also depends on this same model-dependent rate of upwelling of deep ocean anomalies: models with a more vigorous meridional circulation will more rapidly dissipate any deep ocean temperature anomalies, while models with a weaker circulation will tend to have more persistent deep ocean temperature anomalies. Nevertheless, insofar as representation of ocean temperatures in climate models remains imperfect (see, for example, Pohlmann et al. 2009; Smith et al. 2013; Yeager et al. 2018), we expect that there will be some irreducible uncertainty in the Southern Ocean surface energy budget over some timescale in all models. Such uncertainty further increases uncertainty in the transient climate response, as Southern Ocean processes determine the rate of deep ocean heat uptake and, therefore, the rate at which the globe warms in response to anthropogenic greenhouse gas emissions.

Our findings suggest that the Southern Ocean is the primary locale where persisting deep ocean anomalies continue to impact the surface climate over centennial (and longer) time scales. Previous studies have also pointed to the Southern Ocean as being a key site where deep and intermediate-depth ocean processes impact surface climate, through upwelling (Lumpkin and Speer 2007; Talley 2013; Tamsitt et al. 2017) or internal variability (Latif et al. 2013; Behrens et al. 2016; Zhang et al. 2019). Because the Southern Ocean is a central player in global heat and carbon uptake, which together govern how the climate system evolves, deep and intermediate-depth Southern Ocean processes that govern the rate of uptake also have the potential to impact secular climate trends over long timescales (see, e.g., Morrison et al. 2013; Marshall and Zanna 2014; Exarchou et al. 2015).

Surprisingly, we do not find that deep ocean temperature anomalies impact the Northern Hemisphere oceans, particularly the Arctic, over such long time scales. We submit that this is because deep ocean temperature anomalies in the Arctic basin do not have a ready pathway to upwell to the surface, as ocean density stratification is particularly strong under perennial sea ice cover (due to the presence of the cold halocline; see Aagaard et al. 1981). Furthermore, deep and intermediate convection in the North Atlantic tends to bring atmospheric anomalies to depth (where they flow equatorward in the deep branch of the upper cell; Peixoto and Oort 1992; Buckley and Marshall 2016), rather than bringing deep ocean anomalies up to the surface as occurs in the Southern Ocean. This behavior highlights the unique features of the Southern Ocean, particularly the upwelling branch contained therein, which closes the oceanic meridional overturning circulation (Marshall and Speer 2012) and transports anomalies from the deep ocean to the surface.

Our analysis of the CanESM2 large ensemble corroborates the results of Hawkins et al. (2016), who also showed that varying ocean initial conditions increased variance in a large ensemble, albeit in one utilizing an Earth system Model of Intermediate Complexity, not a full ESM. While Hawkins et al. (2016) predominantly focus on the North Atlantic, and how initializing the model in different phases of the Atlantic Multidecadal Oscillation impacts Northern Hemisphere surface climate over multidecadal time scales, our work suggests that it is the Southern Ocean where the impact of ocean initial conditions on ensemble variance persists over centennial time scales. We hypothesize that this difference may be due to the substantial multidecadal periodicity in the strength of the Atlantic meridional overturning circulation in the EMIC utilized by Hawkins et al. (2016). Because CanESM2 does not display such regular, multidecadal variability in the strength of the global overturning circulation (as described in Behrens et al. 2016), the impact of ocean initial conditions in our large ensemble depends less on the phase of coupled modes of variability, and more on the persistence of deep ocean temperatures.

Because temperature anomalies associated with ocean initial conditions can contribute substantially to ensemble variance in surface climate, potentially over very long time scales in the Southern Ocean as shown in this study, we suggest that it would be prudent to consider which ocean states are used to initialize a large ensemble. Our results indicate that an ensemble generated from a sampling of ocean initial states, spanning the full range of possible states a given model can produce over a long control run, is necessary for generating maximum ensemble variance, if that were the goal. However, the precise way to sample ocean initial conditions in order to generate such maximum ensemble variance remains unexplored, and only a few studies have quantified variability in deep ocean heat content in models and observations (see, for example, Santer et al. 1995; Häkkinen et al. 2013; Palter et al. 2014; Palmer et al. 2017). On the other hand, a more limited set of ocean initial states may be preferable if some aspect of the ocean state is well constrained, such as the phase of the Atlantic Multidecadal Oscillation or the Pacific Decadal Oscillation, for example. We suggest that the choice of ocean initial states is an important component of ensemble design, and this choice should reflect the goals of the ensemble.

Before concluding it is important to acknowledge that while variance in the ocean initial state continues to generate ensemble variance in the Southern Ocean surface energy budget over long time scales, the impacts of different ocean initial conditions on multidecadal and centennial timescale trends are relatively small over the rest of the globe in the CanESM2 large ensemble. Indeed, the impact of different ocean initial conditions on the global mean surface temperature and precipitation is not discernible beyond the first decade following ensemble initialization (Figs 12a and 12b, respectively); even Arctic and Antarctic sea ice area show little sensitivity to ocean initial conditions beyond the first several decades following model initialization (Figs 12c and

12d, respectively). And, even over the Southern Ocean, where ocean initial conditions continue to impact surface fluxes over long time scales, we do not find systematic impacts of these on local atmospheric circulation features, such as jet position, the westerly wind maximum, and sea level pressure. We therefore conclude that because the variance attributable to ocean initial conditions is low over much of the upper ocean, apart from the Southern Ocean, and because the atmosphere is highly effective at generating variability, it is possible that centennial time scale projections of most quantities may be robust to the choice of the ocean initial state. We also must note that over such long time scales, uncertainty due to internal variability (whether attributable to macro- or micro-initialization) is small compared to the magnitude of the forced response (as evident in Fig 12; also see Deser et al. 2012; Kay et al. 2015) and, for most quantities, is generally smaller than other sources of uncertainty (including uncertainties in model physics and future emissions scenario; see Hawkins and Sutton 2009).

Finally, we conclude with some caveats of the analysis we've presented here. First, our results rely on a large ensemble that utilizes a single global climate model, the CanESM2. As we discuss above, it is likely that some of our findings are model-dependent. This includes the magnitude of the relationship between deep ocean temperatures and Southern Ocean heat uptake, and how the phasing of coupled variability modes affects model evolution (recall differences between the CanESM2 large ensemble and that of Hawkins et al. 2016, as discussed above). Furthermore, we point out that the creators of the CanESM2 large ensemble did not endeavor to maximize ensemble variance by choosing a range of ocean initial conditions from which to branch their micro-ensembles. Since the large ensemble analyzed in our study was one of convenience, rather than one of design, the fraction of ensemble variance attributable to ocean initial conditions reported here should not be interpreted as an upper bound of this quantity. Further study will be necessary to understand exactly how large this upper bound in ensemble variance might be. Despite these caveats, we contend that as long as there are uncertainties in reckoning the ocean state, these will likely contribute to irreducible uncertainty for future climate projections, especially over the Southern Ocean.

Acknowledgments. All authors acknowledge the CLIVAR Large Ensembles project for providing the model output used in this study. We acknowledge Environment and Climate Change Canada's Canadian Centre for Climate Modelling and Analysis for executing and making available the CanESM2 large ensemble simulations, and the Canadian Sea Ice and Snow Evolution (CanSISE) Network for proposing the simulations. The work of LMP is funded by an award from the US National Science Foundation to Columbia University.

References

Aagaard, K., L. Coachman, and E. Carmack, 1981: On the halocline of the arctic ocean. *Deep Sea Research Part A. Oceanographic Research Papers*, **28 (6)**, 529–545.

Arora, V., and Coauthors, 2011: Carbon emission limits required to satisfy future representative concentration pathways of greenhouse gases. *Geophysical Research Letters*, **38 (5)**.

Athanasiadis, P. J., S. Yeager, Y.-O. Kwon, A. Bellucci, D. W. Smith, and S. Tibaldi, 2020: Decadal predictability of north atlantic blocking and the nao. *npj Climate and Atmospheric Science*, **3 (1)**, 1–10.

Behrens, E., G. Rickard, O. Morgenstern, T. Martin, A. Osprey, and M. Joshi, 2016: Southern Ocean deep convection in global climate models: A driver for variability of subpolar gyres and Drake Passage transport on decadal timescales. *Journal of Geophysical Research: Oceans*, **121**, 3905–3925.

Bellenger, H., É. Guilyardi, J. Leloup, M. Lengaigne, and J. Vialard, 2014: Enso representation in climate models: From cmip3 to cmip5. *Climate Dynamics*, **42 (7)**, 1999–2018.

Bellucci, A., and Coauthors, 2013: Decadal climate predictions with a coupled oagcm initialized with oceanic reanalyses. *Climate dynamics*, **40 (5-6)**, 1483–1497.

Boé, J., A. Hall, and X. Qu, 2009: Deep ocean heat uptake as a major source of spread in transient climate change simulations. *Geophysical Research Letters*, **36 (22)**.

Buckley, M. W., and J. Marshall, 2016: Observations, inferences, and mechanisms of the atlantic meridional overturning circulation: A review. *Reviews of Geophysics*, **54 (1)**, 5–63.

Cavalieri, D., C. Parkinson, P. Gloersen, and H. Zwally, 1996, updated yearly: Sea ice concentrations from Nimbus-7 SMMR and DMSP SSM/I-SSMIS passive microwave data, version 1. NASA National Snow and Ice Data Center Distributed Archive Center.

Chikamoto, Y., and Coauthors, 2013: An overview of decadal climate predictability in a multi-model ensemble by climate model miroc. *Climate Dynamics*, **40 (5-6)**, 1201–1222.

Christian, J., and Coauthors, 2010: The global carbon cycle in the canadian earth system model (canesm1): Preindustrial control simulation. *Journal of Geophysical Research: Biogeosciences*, **115 (G3)**.

Deser, C., A. Phillips, V. Bourdette, and H. Teng, 2012: Uncertainty in climate change projections: the role of internal variability. *Climate dynamics*, **38 (3-4)**, 527–546.

Deser, C., A. S. Phillips, M. A. Alexander, and B. V. Smoliak, 2014: Projecting north american climate over the next 50 years: Uncertainty due to internal variability. *Journal of Climate*, **27 (6)**, 2271–2296.

Deser, C., and Coauthors, 2020: Insights from earth system model initial-condition large ensembles and future prospects. *Nature Climate Change*, 1–10.

Ding, Q., and Coauthors, 2017: Influence of high-latitude atmospheric circulation changes on summertime arctic sea ice. *Nature Climate Change*, **7 (4)**, 289–295.

Dunstone, N., D. Smith, and R. Eade, 2011: Multi-year predictability of the tropical atlantic atmosphere driven by the high latitude north atlantic ocean. *Geophysical Research Letters*, **38 (14)**.

England, M., A. Jahn, and L. Polvani, 2019: Nonuniform contribution of internal variability to recent arctic sea ice loss. *Journal of Climate*, **32 (13)**, 4039–4053.

Exarchou, E., T. Kuhlbrodt, J. M. Gregory, and R. S. Smith, 2015: Ocean heat uptake processes: A model intercomparison. *Journal of Climate*, **28 (2)**, 887–908.

Flato, G., and Coauthors, 2014: Evaluation of climate models. *Climate change 2013: the physical science basis. Contribution of Working Group I to the Fifth Assessment Report of the Intergovernmental Panel on Climate Change*, Cambridge University Press, 741–866.

Frölicher, T. L., J. L. Sarmiento, D. J. Paynter, J. P. Dunne, J. P. Krasting, and M. Winton, 2015: Dominance of the southern ocean in anthropogenic carbon and heat uptake in cmip5 models. *Journal of Climate*, **28 (2)**, 862–886.

Gent, P., and J. McWilliams, 1992: Isopycnal mixing in ocean circulation models. *Journal of Physical Oceanography*, **20**, 150–155.

Griffies, S. M., and K. Bryan, 1997: Predictability of north atlantic multidecadal climate variability. *Science*, **275 (5297)**, 181–184.

Gupta, A. S., L. C. Muir, J. N. Brown, S. J. Phipps, P. J. Durack, D. Monselesan, and S. E. Wijffels, 2012: Climate drift in the cmip3 models. *Journal of Climate*, **25 (13)**, 4621–4640.

Hagos, S. M., L. R. Leung, J.-H. Yoon, J. Lu, and Y. Gao, 2016: A projection of changes in landfalling atmospheric river frequency and extreme precipitation over western north america from the large ensemble cesm simulations. *Geophysical Research Letters*, **43 (3)**, 1357–1363.

Häkkinen, S., P. B. Rhines, and D. L. Worthen, 2013: Northern north atlantic sea surface height and ocean heat content variability. *Journal of Geophysical Research: Oceans*, **118 (7)**, 3670–3678.

Hawkins, E., R. S. Smith, J. M. Gregory, and D. A. Stainforth, 2016: Irreducible uncertainty in near-term climate projections. *Climate Dynamics*, **46 (11-12)**, 3807–3819.

Hawkins, E., and R. Sutton, 2009: The potential to narrow uncertainty in regional climate predictions. *Bulletin of the American Meteorological Society*, **90 (8)**, 1095–1108.

Hobbs, W., M. D. Palmer, and D. Monselesan, 2016: An energy conservation analysis of ocean drift in the cmip5 global coupled models. *Journal of Climate*, **29 (5)**, 1639–1653.

Jahn, A., J. E. Kay, M. M. Holland, and D. M. Hall, 2016: How predictable is the timing of a summer ice-free arctic? *Geophysical Research Letters*, **43 (17)**, 9113–9120.

Kang, S. M., C. Deser, and L. M. Polvani, 2013: Uncertainty in climate change projections of the hadley circulation: The role of internal variability. *Journal of Climate*, **26 (19)**, 7541–7554.

Kay, J., and Coauthors, 2015: The Community Earth System Model (CESM) Large Ensemble project: A community resource for studying climate change in the presence of internal climate variability. *Bulletin of the American Meteorological Society*, **96**, 1333–1349.

Khairoutdinov, M., and Y. Kogan, 2000: A new cloud physics parameterization in a large-eddy simulation model of marine stratocumulus. *Monthly weather review*, **128 (1)**, 229–243.

Kirchmeier-Young, M. C., F. W. Zwiers, and N. P. Gillett, 2017: Attribution of extreme events in arctic sea ice extent. *Journal of Climate*, **30 (2)**, 553–571.

Kuhlbrodt, T., and J. Gregory, 2012: Ocean heat uptake and its consequences for the magnitude of sea level rise and climate change. *Geophysical Research Letters*, **39 (18)**.

Large, W. G., J. C. McWilliams, and S. C. Doney, 1994: Oceanic vertical mixing: A review and a model with a nonlocal boundary layer parameterization. *Reviews of Geophysics*, **32 (4)**, 363–403.

Latif, M., and N. S. Keenlyside, 2011: A perspective on decadal climate variability and predictability. *Deep Sea Research Part II: Topical Studies in Oceanography*, **58 (17-18)**, 1880–1894.

Latif, M., T. Martin, and W. Park, 2013: Southern ocean sector centennial climate variability and recent decadal trends. *Journal of Climate*, **26 (19)**, 7767–7782.

Li, J., and H. Barker, 2005: A radiation algorithm with correlated-k distribution. part i: Local thermal equilibrium. *Journal of the atmospheric sciences*, **62 (2)**, 286–309.

Lovenduski, N. S., G. A. McKinley, A. R. Fay, K. Lindsay, and M. C. Long, 2016: Partitioning uncertainty in ocean carbon uptake projections: Internal variability, emission scenario, and model structure. *Global Biogeochemical Cycles*, **30 (9)**, 1276–1287.

Lumpkin, R., and K. Speer, 2007: Global ocean meridional overturning. *Journal of Physical Oceanography*, **37 (10)**, 2550–2562.

Ma, X., K. von Salzen, and J. Cole, 2010: Constraints on interactions between aerosols and clouds on a global scale from a combination of modis-ceres satellite data and climate simulations. *Atmospheric Chemistry and Physics*, **10 (20)**, 9851.

Maher, N., and Coauthors, 2019: The max planck institute grand ensemble: Enabling the exploration of climate system variability. *Journal of Advances in Modeling Earth Systems*, **11 (7)**, 2050–2069.

Marshall, D. P., and L. Zanna, 2014: A conceptual model of ocean heat uptake under climate change. *Journal of Climate*, **27 (22)**, 8444–8465.

Marshall, J., and K. Speer, 2012: Closure of the meridional overturning circulation through Southern Ocean upwelling. *Nature Geoscience*, **5**, 171–180.

Meehl, G. A., J. M. Arblaster, C. M. Bitz, C. T. Chung, and H. Teng, 2016: Antarctic sea-ice expansion between 2000 and 2014 driven by tropical pacific decadal climate variability. *Nature Geoscience*, **9 (8)**, 590–595.

Meehl, G. A., and Coauthors, 2014: Decadal climate prediction: an update from the trenches. *Bulletin of the American Meteorological Society*, **95 (2)**, 243–267.

Mochizuki, T., and Coauthors, 2012: Decadal prediction using a recent series of miroc global climate models. *Journal of the Meteorological Society of Japan. Ser. II*, **90**, 373–383.

Morrison, A., O. Saenko, A. M. Hogg, and P. Spence, 2013: The role of vertical eddy flux in southern ocean heat uptake. *Geophysical Research Letters*, **40 (20)**, 5445–5450.

Palmer, M., and Coauthors, 2017: Ocean heat content variability and change in an ensemble of ocean reanalyses. *Climate Dynamics*, **49 (3)**, 909–930.

Palter, J. B., S. M. Griffies, B. L. Samuels, E. D. Galbraith, A. Gnanadesikan, and A. Klocker, 2014: The deep ocean buoyancy budget and its temporal variability. *Journal of climate*, **27 (2)**, 551–573.

Peixoto, J., and A. Oort, 1992: *Physics of Climate*. American Institute of Physics.

Pohlmann, H., J. H. Jungclaus, A. Köhl, D. Stammer, and J. Marotzke, 2009: Initializing decadal climate predictions with the gecco oceanic synthesis: Effects on the north atlantic. *Journal of Climate*, **22 (14)**, 3926–3938.

Rintoul, S. R., 1991: South atlantic interbasin exchange. *Journal of Geophysical Research: Oceans*, **96 (C2)**, 2675–2692.

Rodwell, M. J., D. P. Rowell, and C. K. Folland, 1999: Oceanic forcing of the wintertime north atlantic oscillation and european climate. *Nature*, **398 (6725)**, 320–323.

Santer, B. D., U. Mikolajewicz, W. Brüggemann, U. Cubasch, K. Hasselmann, H. Höck, E. Maier-Reimer, and T. M. Wigley, 1995: Ocean variability and its influence on the detectability of greenhouse warming signals. *Journal of Geophysical Research: Oceans*, **100 (C6)**, 10 693–10 725.

Screen, J. A., C. Deser, I. Simmonds, and R. Tomas, 2014: Atmospheric impacts of arctic sea-ice loss, 1979–2009: Separating forced change from atmospheric internal variability. *Climate dynamics*, **43 (1-2)**, 333–344.

Shi, J.-R., S.-P. Xie, and L. D. Talley, 2018: Evolving relative importance of the southern ocean and north atlantic in anthropogenic ocean heat uptake. *Journal of Climate*, **31 (18)**, 7459–7479.

Simpson, I. R., S. G. Yeager, K. A. McKinnon, and C. Deser, 2019: Decadal predictability of late winter precipitation in western europe through an ocean–jet stream connection. *Nature Geoscience*, **12 (8)**, 613–619.

Singh, H., L. M. Polvani, and P. J. Rasch, 2019: Antarctic sea ice expansion, driven by internal variability, in the presence of increasing atmospheric co2. *Geophysical Research Letters*, **46 (24)**, 14 762–14 771.

Smith, D. M., R. Eade, and H. Pohlmann, 2013: A comparison of full-field and anomaly initialization for seasonal to decadal climate prediction. *Climate Dynamics*, **41 (11-12)**, 3325–3338.

Stainforth, D. A., M. R. Allen, E. R. Tredger, and L. A. Smith, 2007: Confidence, uncertainty and decision-support relevance in climate predictions. *Philosophical Transactions of the Royal Society A: Mathematical, Physical and Engineering Sciences*, **365 (1857)**, 2145–2161.

Sutton, R., and P.-P. Mathieu, 2002: Response of the atmosphere-ocean mixed-layer system to anomalous ocean heat-flux convergence. *Quarterly Journal of the Royal Meteorological Society*, **128**, 1259–1275.

Swart, N. C., J. C. Fyfe, E. Hawkins, J. E. Kay, and A. Jahn, 2015: Influence of internal variability on Arctic sea-ice trends. *Nature Climate Change*, **5 (2)**, 86.

Talley, L. D., 2013: Closure of the global overturning circulation through the indian, pacific, and southern oceans: Schematics and transports. *Oceanography*, **26 (1)**, 80–97.

Tamsitt, V., and Coauthors, 2017: Spiraling pathways of global deep waters to the surface of the southern ocean. *Nature communications*, **8 (1)**, 1–10.

Taylor, K., R. Stouffer, and G. Meehl, 2012: An overview of CMIP5 and the experiment design. *Bulletin of the American Meteorological Society*, **93**, 485–498.

Thomas, J. L., D. W. Waugh, and A. Gnanadesikan, 2015: Southern hemisphere extratropical circulation: Recent trends and natural variability. *Geophysical Research Letters*, **42 (13)**, 5508–5515.

von Salzen, K., and Coauthors, 2013: The canadian fourth generation atmospheric global climate model (canam4). part i: representation of physical processes. *Atmosphere-Ocean*, **51 (1)**, 104–125.

Von Storch, H., and F. W. Zwiers, 2001: *Statistical analysis in climate research*. Cambridge university press.

Wagner, T. J., and I. Eisenman, 2015: How climate model complexity influences sea ice stability. *Journal of Climate*, **28 (10)**, 3998–4014.

Wettstein, J. J., and C. Deser, 2014: Internal variability in projections of twenty-first-century arctic sea ice loss: Role of the large-scale atmospheric circulation. *Journal of Climate*, **27 (2)**, 527–550.

Yang, D., and O. A. Saenko, 2012: Ocean heat transport and its projected change in canesm2. *Journal of climate*, **25 (23)**, 8148–8163.

Yeager, S., and J. Robson, 2017: Recent progress in understanding and predicting atlantic decadal climate variability. *Current Climate Change Reports*, **3 (2)**, 112–127.

Yeager, S., and Coauthors, 2018: Predicting near-term changes in the earth system: A large ensemble of initialized decadal prediction simulations using the community earth system model. *Bulletin of the American Meteorological Society*, **99 (9)**, 1867–1886.

Yim, B. Y., M. Kwon, H. S. Min, and J.-S. Kug, 2015: Pacific decadal oscillation and its relation to the extratropical atmospheric variation in cmip5. *Climate Dynamics*, **44 (5-6)**, 1521–1540.

Zhang, L., T. Delworth, W. Cooke, and X. Yang, 2019: Natural variability of Southern Ocean convection as a driver of observed climate trends. *Nature Climate Change*, **9 (1)**, 59.

LIST OF FIGURES

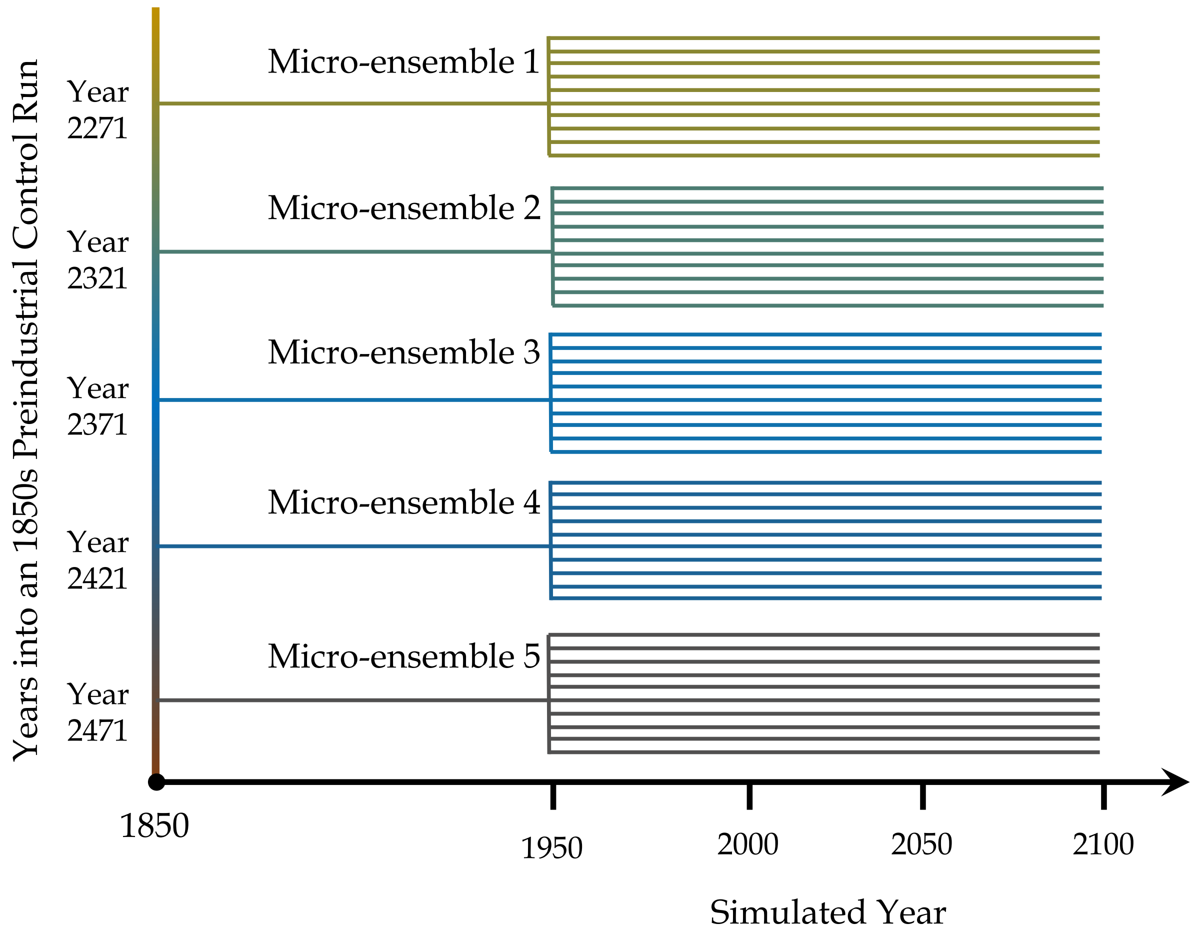

FIG. 1. Initialization structure of the 50-member CanESM2 large ensemble. Five runs were branched at 50-year intervals from the 1850 Pre-industrial Control, and each was subjected to identical historical forcings from the period 1850 to 1950. At year 1950, each of the five runs was perturbed with ten distinct random atmospheric micro-perturbations, which created ten ensemble members per branched run. Each of these micro-ensembles of ten members were subjected to identical historical forcings (from the period 1950 to 2005), and then subject to the RCP8.5 future scenario forcing (Taylor et al. 2012) to year 2100.

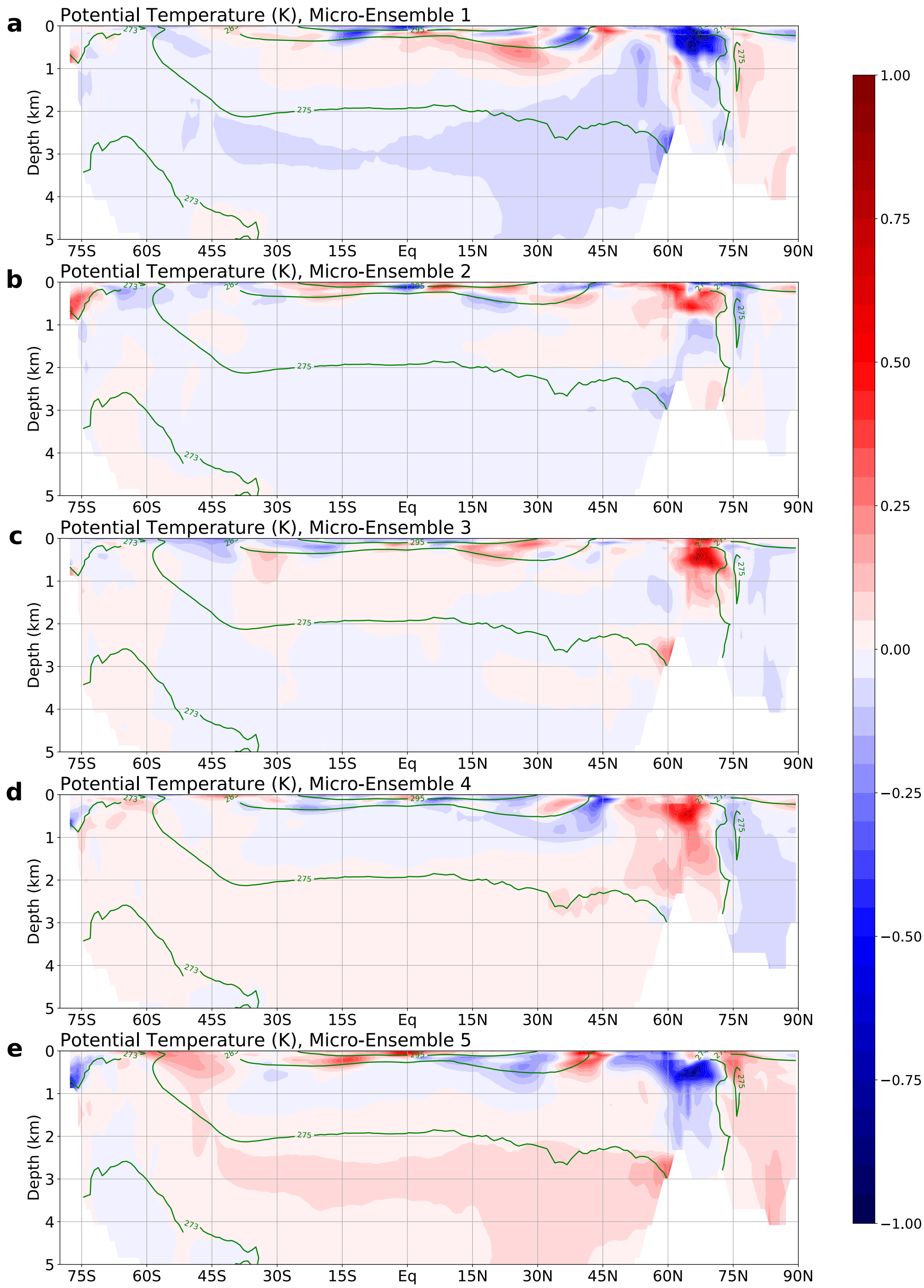

864 FIG. 2. Zonal mean ocean potential anomaly (K; shading) in each micro-ensemble at year 1950 relative to the
865 mean potential temperature (contours at 273, 275, 285, and 295 K) in the full ensemble at year 1950.

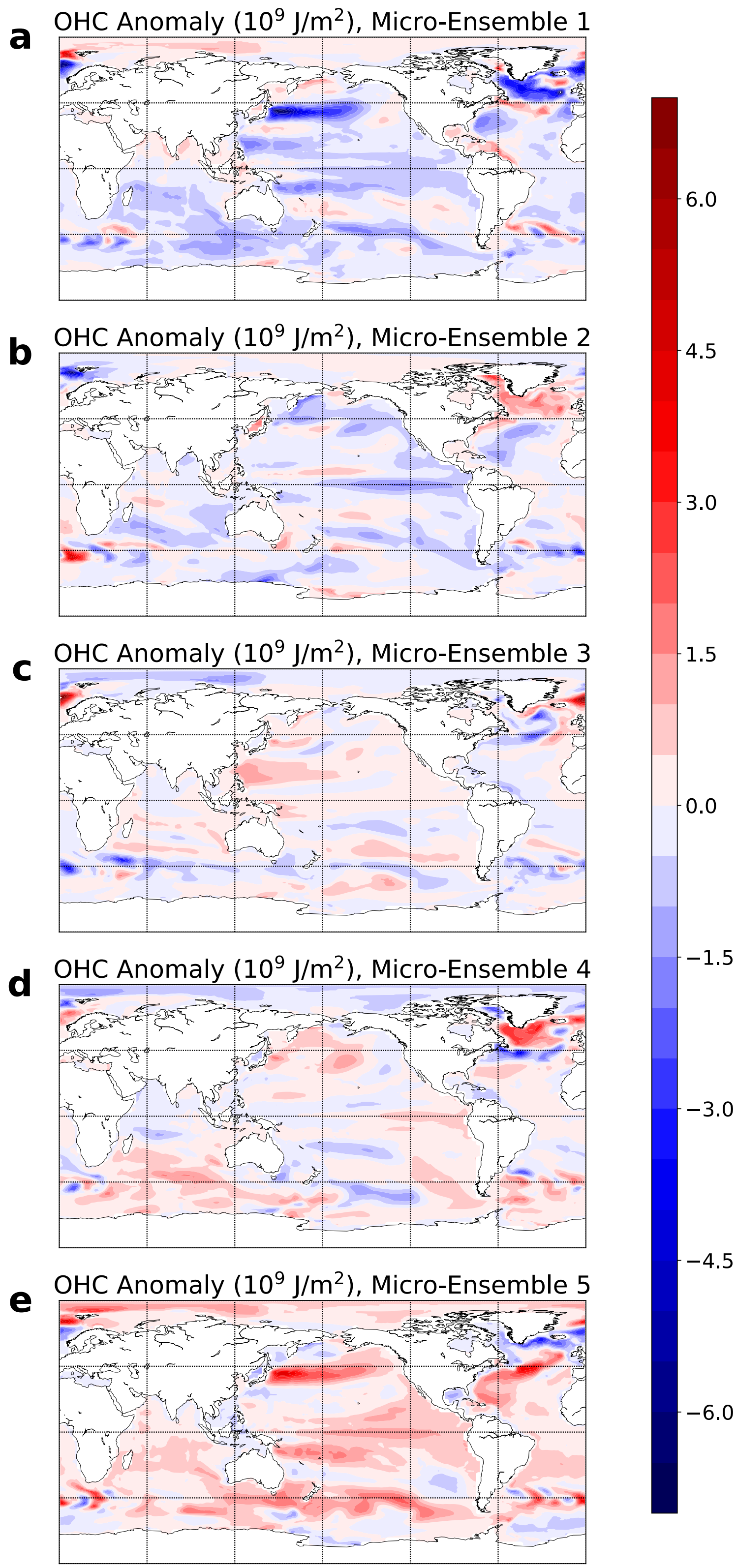

FIG. 3. Anomaly in ocean heat content per unit area (10^9 J m^{-}2) at year 1950 in (a-e) micro-ensembles 1 through 5, respectively, relative to the mean ocean heat content in the full ensemble at year 1950; in other words, $\overline{OHC_k}(t = 1950) - \overline{OHC}(t = 1950)$.

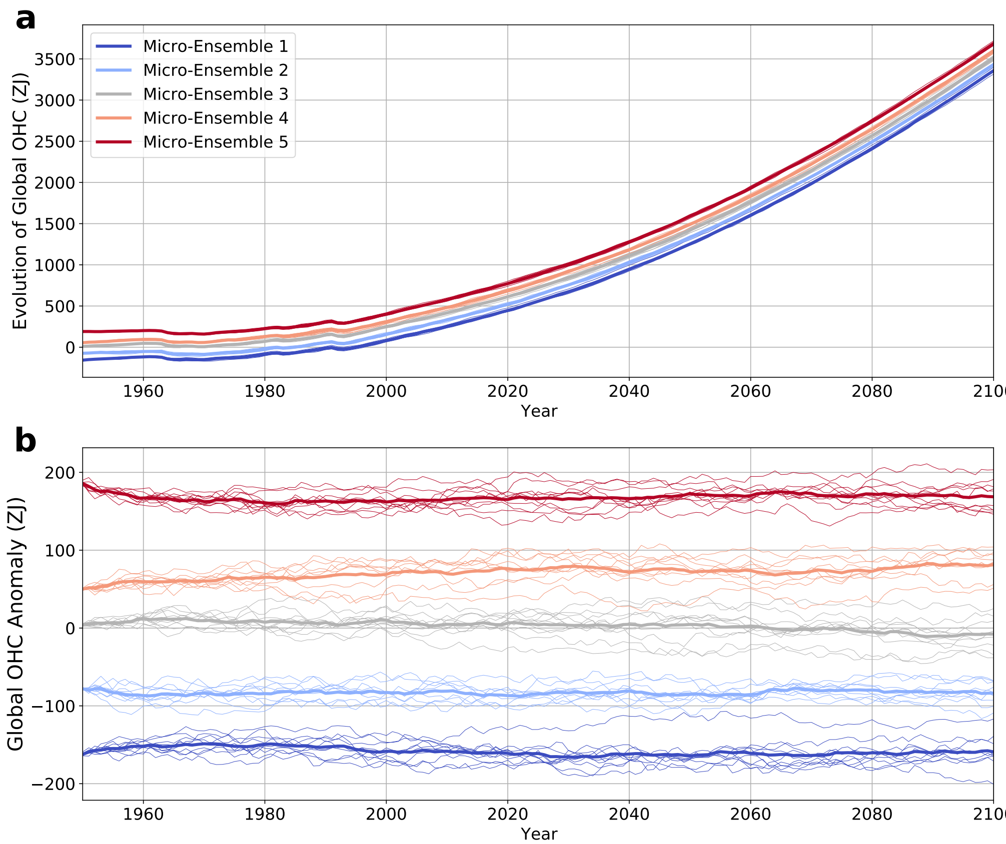

FIG. 4. Evolution of global ocean heat content in the CanESM2 large ensemble, color-coded by micro-ensemble, with thin lines denoting individual ensemble members and thick lines denoting micro-ensemble means ($\overline{OHC_k}(t)$). Shown are the (a) drift-corrected global ocean heat content in each ensemble member (in ZJ), relative to the ensemble-mean global ocean heat content over years 1950 to 1970; and (b) the global ocean heat content anomaly (in ZJ) relative to the yearly ensemble-mean ocean heat content (i.e. $\overline{OHC_k}(t) - \overline{OHC}(t)$ for the k-th micro-ensemble, and $OHC_i(t) - \overline{OHC}(t)$ for the i-th ensemble member). For (a), we drift-correct following the procedure outlined in Gupta et al. (2012).

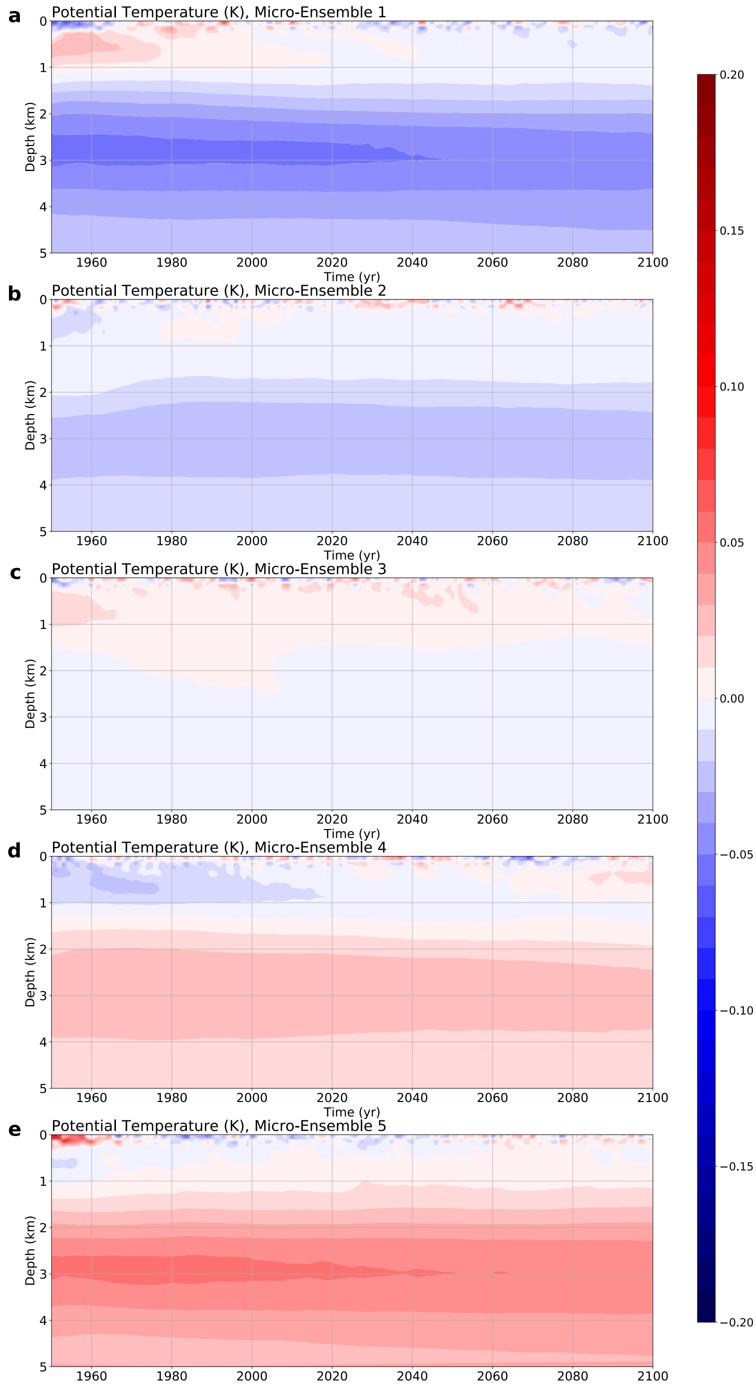

876 FIG. 5. Evolution of the area-weighted, globally-averaged, ocean potential temperature anomaly (K) in each micro-ensemble. The anomaly is computed relative to the global mean potential temperature in the full ensemble each year.

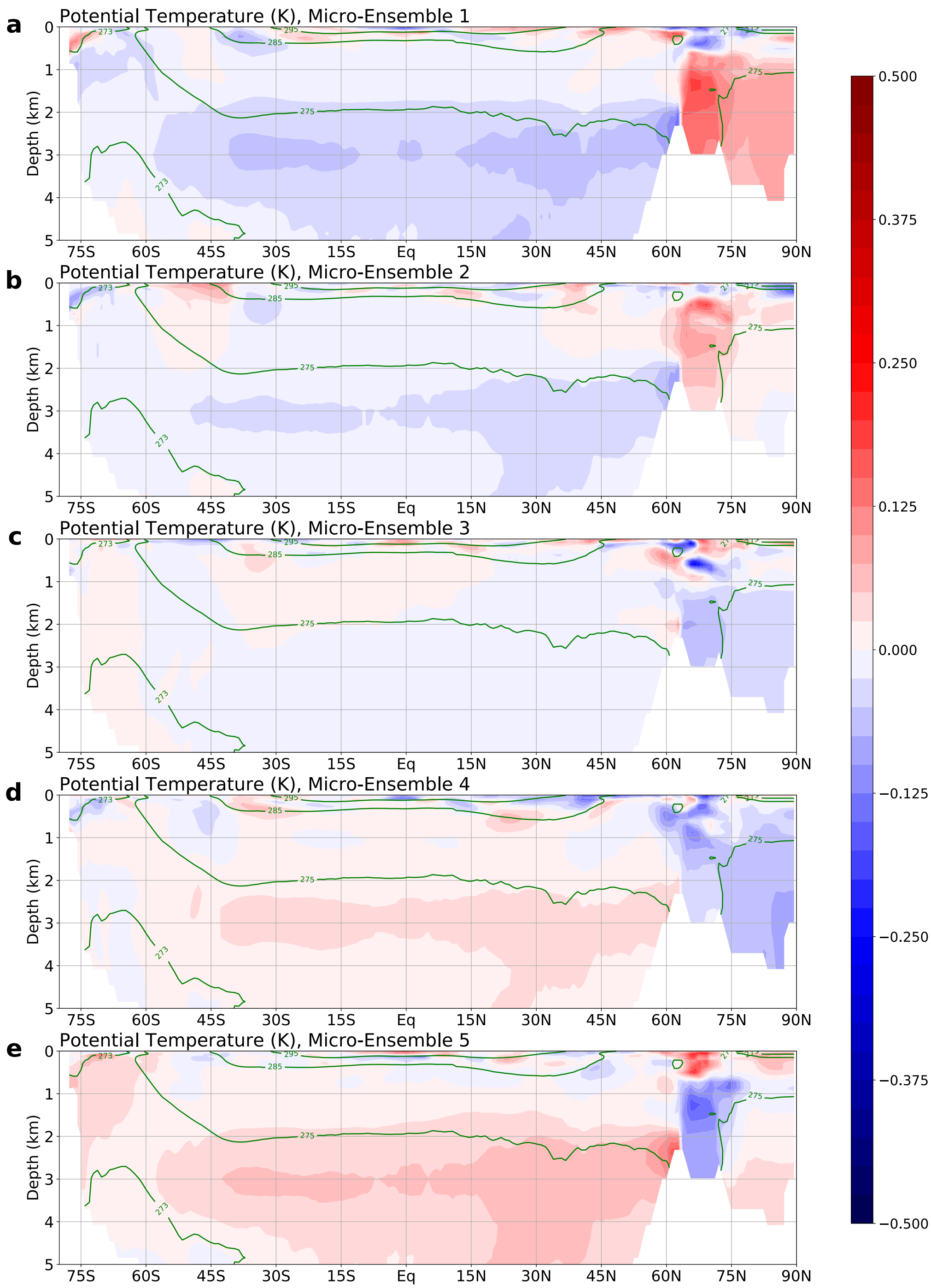

879 FIG. 6. Zonal mean ocean potential anomaly (K; shading) in each micro-ensemble at year 2080 relative to the
880 mean potential temperature (contours at 273, 275, 285, and 295 K) in the full ensemble at year 2080; in other
881 words, $\overline{OHC_k}(t = 2080) - \overline{OHC}(t = 2080)$.

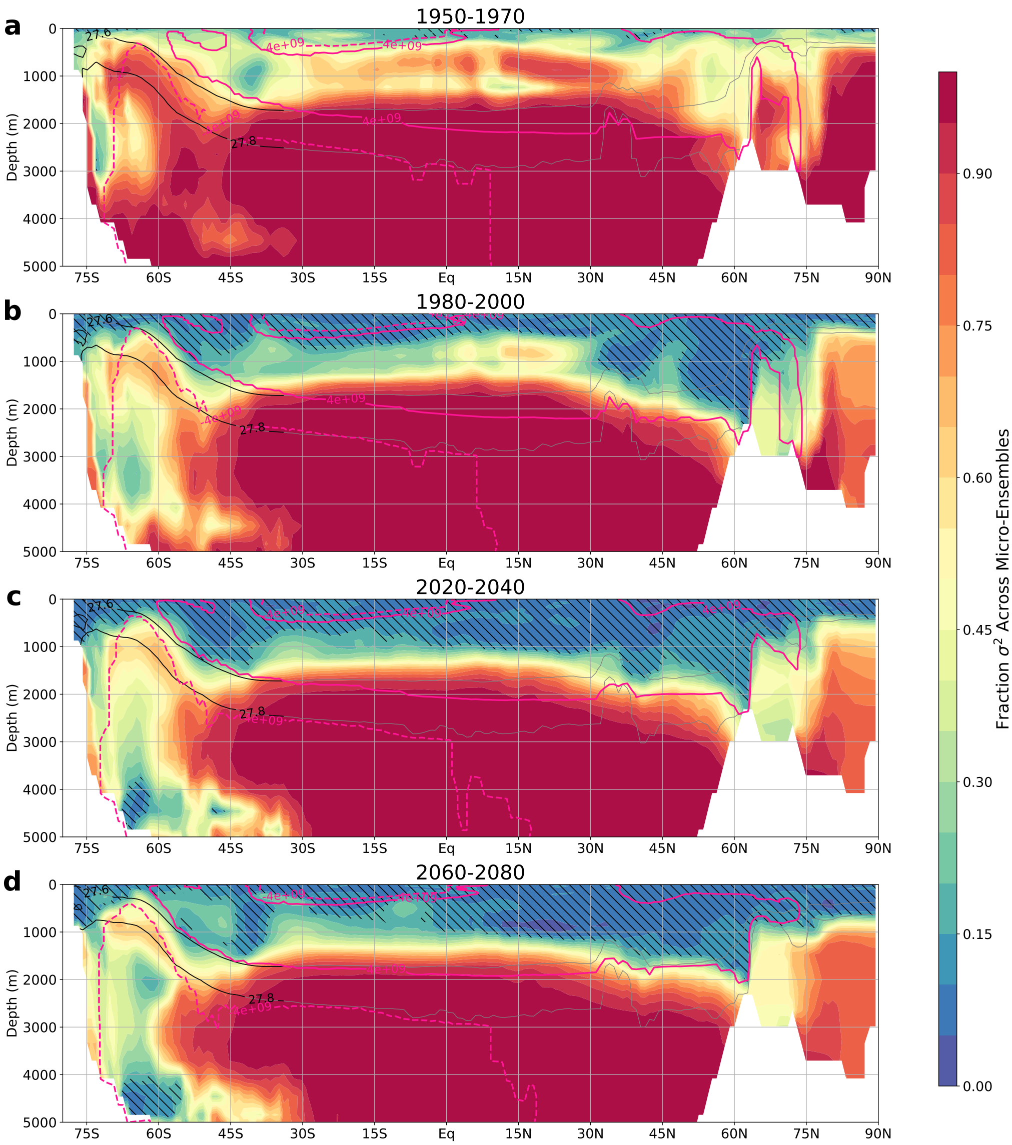

FIG. 7. Fraction of total variance in zonal mean ocean potential temperature attributable to variance between micro-ensembles, $\chi_{OcnICs} = \sigma^2_{\theta,ocean}/\sigma^2_{\theta}$, over four time periods spanning the full 150 years of the experiment: (a) years 1950 to 1970, (b) 1980 to 2000, (c) 2020 to 2040, and (d) 2060 to 2080. Also shown are isopycnal contours (solid lines; at *sigma* levels 27.6 and 27.8 kg m^{-3}) and the ocean meridional mass overturning streamfunction (pink contours at [-4, 4]$\times$ 10^9 kg sec^{-1}). Hatched areas indicate that the fraction of ensemble variance attributable to ocean initial conditions is not statistically distinct from zero at $p < 0.1$.

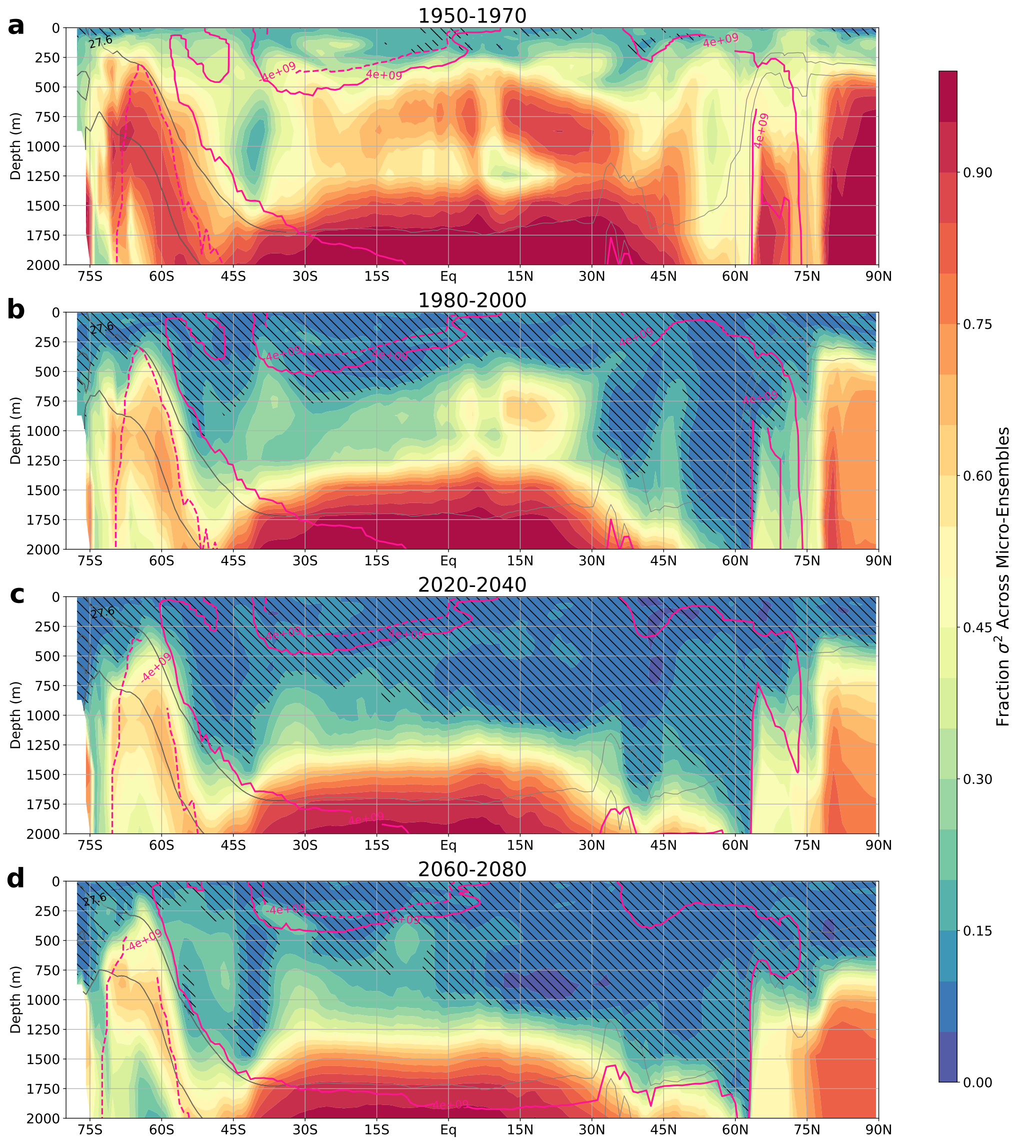

FIG. 8. As for Figure 7, but only including the top 2000 m of the ocean.

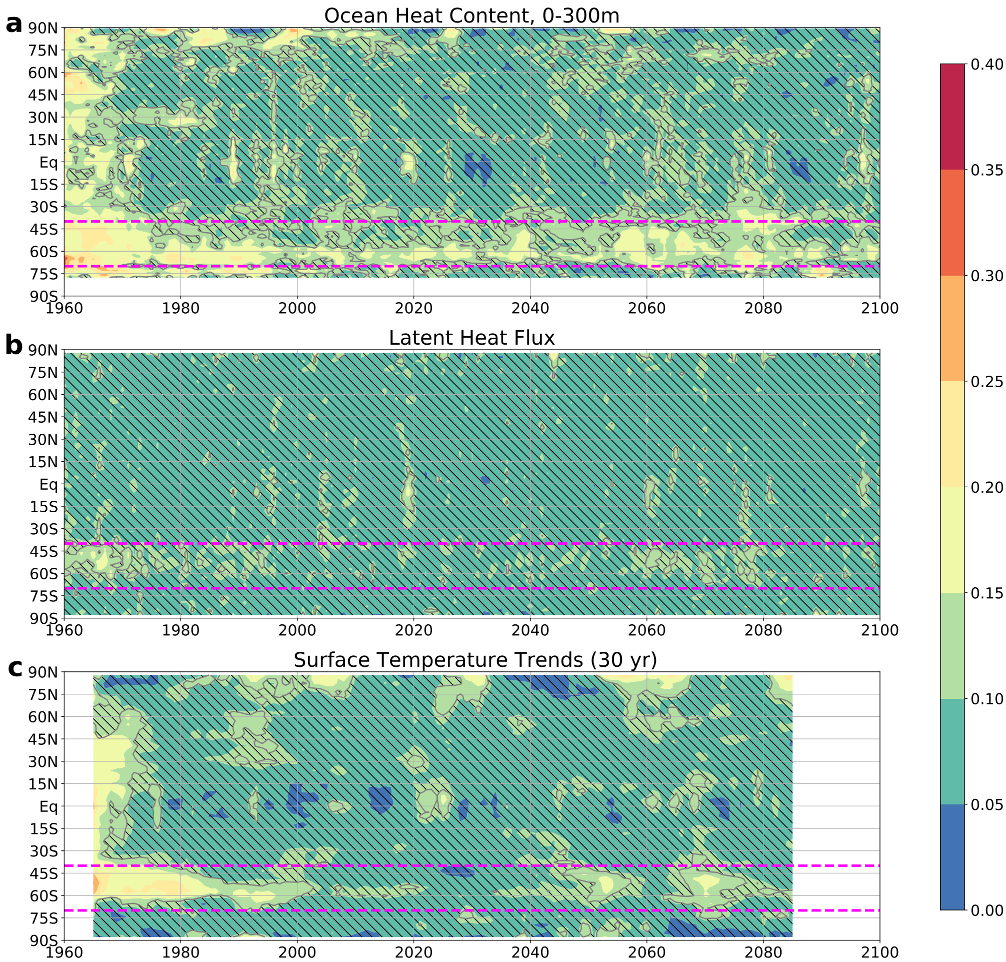

FIG. 9. Zonal mean fraction of ensemble variance in (a) upper 300 m ocean heat content, (b) latent heat flux, and (c) 30-year surface temperature trends, attributable to variance between micro-ensembles ($\chi_{OcnICs} = \sigma^2_{X,ocean}/\sigma^2_X$) over the full 150 years of the ensemble. Hatched areas indicate that the fraction of ensemble variance attributable to ocean initial conditions is not statistically distinct from zero at $p < 0.1$ at more than 25% of the grid cells at that latitude. Dashed horizontal pink lines at 40S and 70S delineate the Southern Ocean.

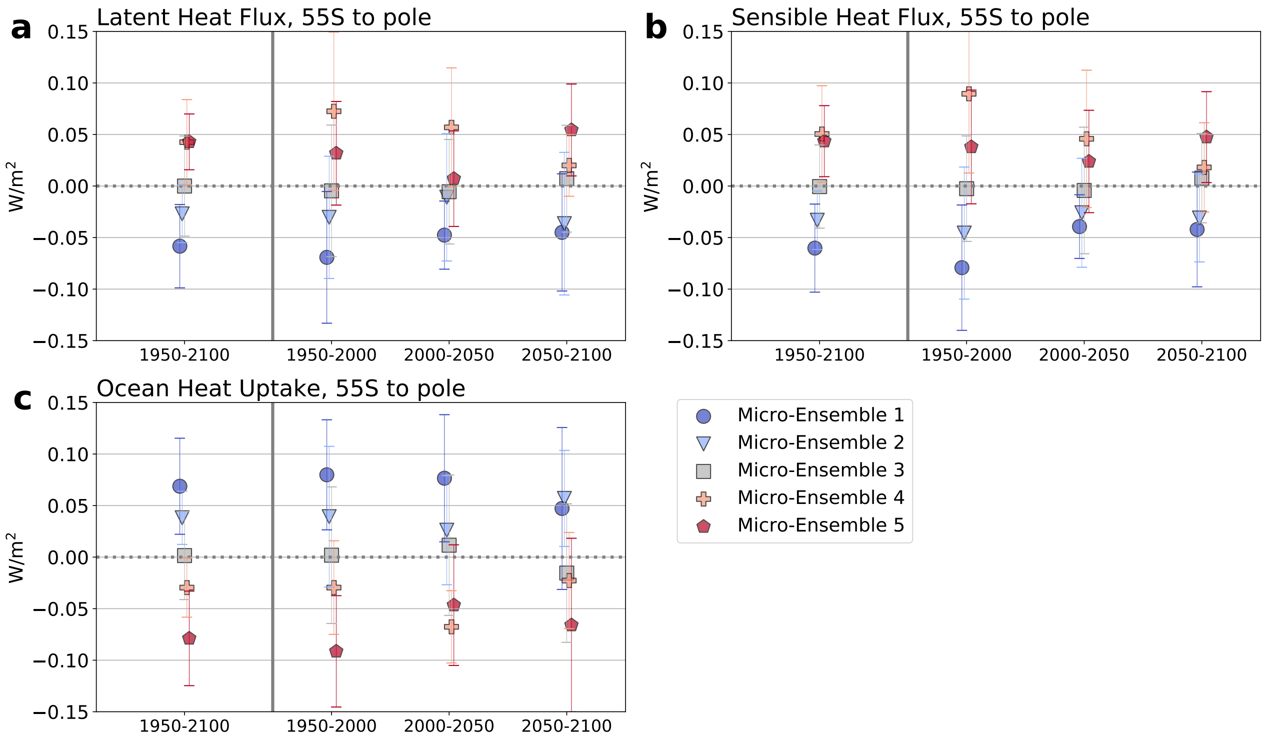

FIG. 10. Micro-ensemble anomalies, in W m^{-2}, in (a) latent heat fluxes, (b) sensible heat fluxes, and (c) ocean heat uptake, all poleward of 55S, in the CanESM2 large ensemble. Anomalies for each micro-ensemble are computed with respect to the mean of the full ensemble (i.e., as $\overline{X_k}(t) - \overline{X}(t)$), and are calculated over four time periods: the full 150 years of the experiment (1950 to 2100), from 1950 to 2000, from 2000 to 2050, and from 2050 to 2100. Over all time periods and for all quantities, the fraction of ensemble variance due to the ocean initial state is statistically significant at $p < 0.1$, with the exception of the sensible heat flux over years 2000 to 2050. Vertical bars indicate the standard deviation within each micro-ensemble (i.e., $\sigma_{X,\ atmos,k}$ for the k-th micro-ensemble).

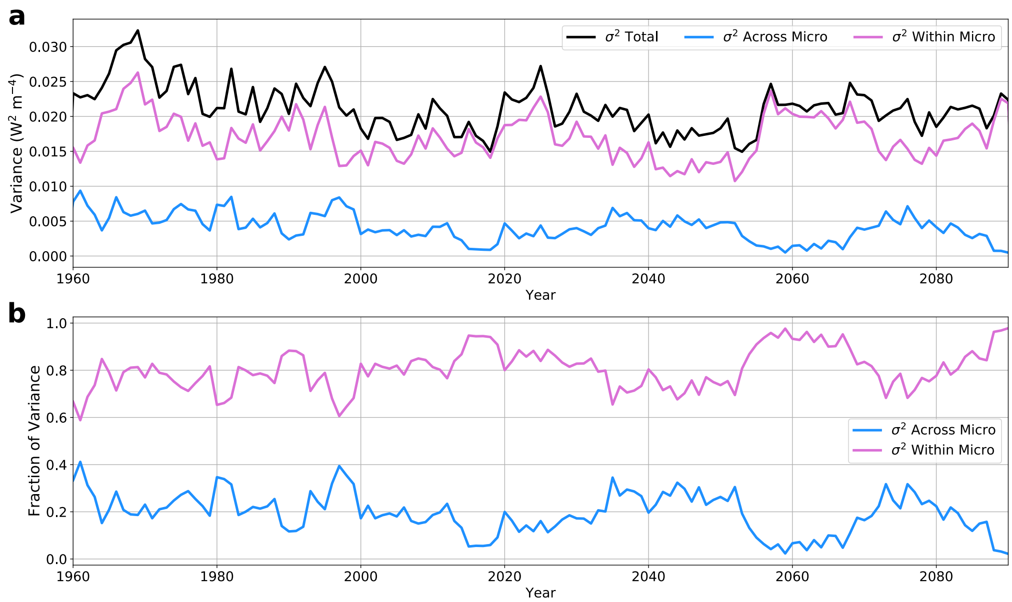

FIG. 11. Ensemble variance in ocean heat uptake poleward of 55S: (a) total ensemble variance over the full 150 years of the experiment (black line), partitioned into the variance between micro-ensembles ($\sigma^2_{OHU,ocean}$; blue line) and within micro-ensembles ($\sigma^2_{OHU,atmos}$; purple line); and (b) fraction of the total ensemble variance between micro-ensembles (blue line) and within micro-ensembles (purple line).

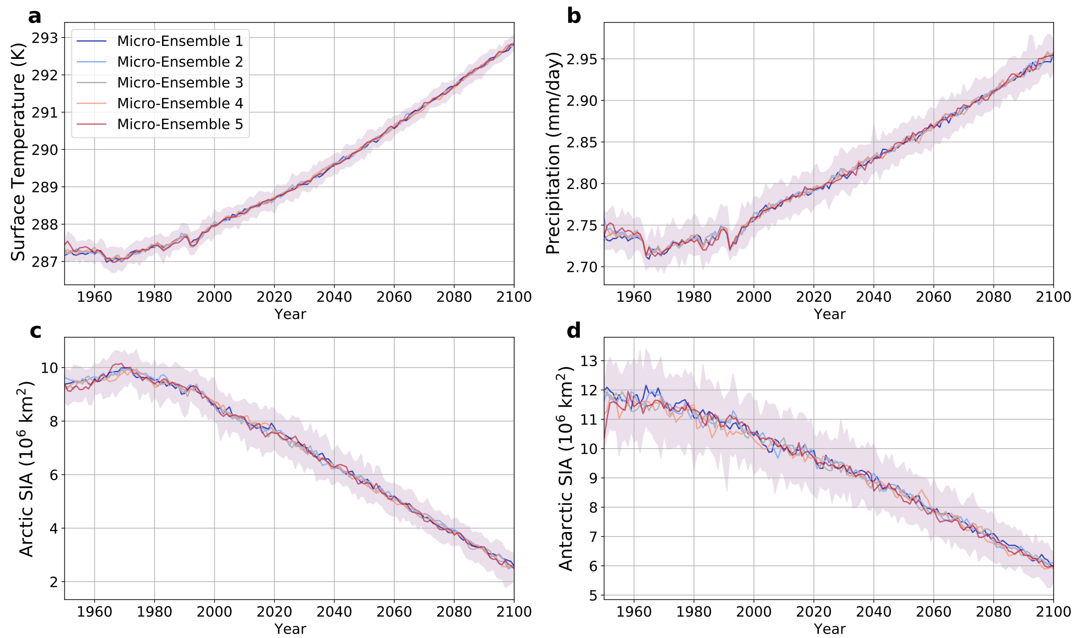

FIG. 12. Evolution of annual mean (a) global surface temperature (in K), (b) global precipitation (in mm/day), (c) Arctic sea ice area (in 10^6 km^2), and (d) Antarctic sea ice area (in 10^6 km^2) in the CanESM2 large ensemble. Color-coded lines show the micro-ensemble means, and the shaded envelopes indicate the range of the annual mean in the full ensemble.